Three-Dimensional Reconstruction and Quantification of Cervical Carcinoma Invasion Fronts From Histological Serial Sections

Ulf-Dietrich Braumann, *Member, IEEE*, Jens-Peer Kuska, *Member, IEEE*, Jens Einenkel, Lars-Christian Horn, Markus Löffler, and Michael Höckel

***Abstract*—The analysis of the three-dimensional (3-D) structure of tumoral invasion fronts of carcinoma of the uterine cervix is the prerequisite for understanding their architectural-functional relationship. The variation range of the invasion patterns known so far reaches from a smooth tumor-host boundary surface to more diffusely spreading patterns, which all are supposed to have a different prognostic relevance. As a very decisive limitation of previous studies, all morphological assessments just could be done verbally referring to single histological sections. Therefore, the intention of this paper is to get an objective quantification of tumor invasion based on 3-D reconstructed tumoral tissue data. The image processing chain introduced here is capable to reconstruct selected parts of tumor invasion fronts from histological serial sections of remarkable extent (90–500 slices). While potentially gaining good accuracy and reasonably high resolution, microtome cutting of large serial sections especially may induce severe artifacts like distortions, folds, fissures or gaps. Starting from stacks of digitized transmitted light color images, an overall of three registration steps are the main parts of the presented algorithm. By this, we achieved the most detailed 3-D reconstruction of the invasion of solid tumors so far. Once reconstructed, the invasion front of the segmented tumor is quantified using discrete compactness.**

***Index Terms*—Biological tissues, image color analysis, image processing, image registration, image segmentation, image shape analysis, scientific visualization, tumors.**

I. Introduction

To our understanding, to really consider volumes but not just single slices is essential in order to get new insight views of tissue organization, e.g., tumor morphology and tumor growth. The three-dimensional (3-D) characterization of invasion patterns of squamos cell carcinoma of the uterine cervix using histological serial sections is a current clinical question. This gives demand for both high level image processing and analysis. Properties of the hitherto observed two-dimensional (2-D) tumor invasion fronts are supposed to have relevance for the further prognosis of the respective patient [1]–[4]. Doing those quantitative analyses in 3-D, a new quality for the structural and morphological assessment of the considered tumors can be expected.

Three-dimensional imaging modalities like computed tomography (CT), cone beam computed tomography (CBCT), nuclear magnetic resonance imaging (MRI), positron emission tomography (PET), single photon emission computed tomography (SPECT), etc. have become state of the art in many fields of medical diagnostics and research. Besides those macroscopic *in vivo* 3-D techniques, for more detailed analyses nondestructive 3-D microscopy is available for *in vitro* (partially applicable *in vivo*), as e.g., scanning transmission ion microscopy (STIM) or particle induced X-ray emission (PIXE), scanning force microscopy (SFM), 3-D electron microscopy (3DEM), miniaturized computed tomography (μCT), miniaturized nuclear magnetic resonance imaging (μMRI) or confocal LASER scanning microscopy (CLSM), etc. For a concise review on current high-resolution imaging techniques of (living) tissue, see [5].

CLSM could be successfully applied on precancerous cervical epithelial lesions [6] both *ex vivo* on biopsies in 3-D, as well as *in vivo* in 2-D using a CLSM-variant referred to as "confocal microendoscope." The limited range of CLSM of about 100, ..., 200 μm is acceptable for these epithelial lesions. The whole epithelium's thickness is 200,..., 300 μm. For the analysis of cervical *tumors*, the CLSM's penetration range unfortunately is too short.

Even though other *in vivo* techniques would be desirable for detailed uterine cervix analyses, spatial resolutions of ≈ 1 mm as achieved e.g., in MRIs from the pelvic region unfortunately do not appear sufficient for conclusions on tumor invasion and infiltration which necessitates resolutions ≤ 0.05 mm, but not far beyond typical cell diameters of ≈ 10 μm. However, for clinical diagnostics of cervical cancer (e.g., tumor staging), MRI and partially CT are indispensable [7], [8] and partially can be used to "predict" histopathologic features. The "ground truth" for tumor typing, however, only can be obtained by histopathology both using visual inspection and especially

Manuscript received December 28, 2004; revised July 12, 2005. This work was supported by the German Research Foundation (DFG) under Grant BIZ-6 1/1-3. The Associate Editor responsible for coordinating the review of this paper and recommending its publication was N. Ayache. *Asterisk indicates corresponding author.*

*U.-D. Braumann is with the Interdisciplinary Center for Bioinformatics, University Leipzig, Härtelstraße 16-18, 04107 Leipzig, Germany (e-mail: braumann@izbi.uni-leipzig.de).

J.-P. Kuska is with the Interdisciplinary Center for Bioinformatics, University Leipzig, 04107 Leipzig, Germany (e-mail: kuska@informatik.uni-leipzig.de).

J. Einenkel and M. Höckel are with the Department of Gynecology and Obstetrics, University Leipzig, 04103 Leipzig, Germany (e-mail: jens.einenkel@medizin.uni-leipzig.de, michael.hoeckel@medizin.uni-leipzig.de).

L.-C. Horn is with the Institute of Pathology, University Leipzig, 04103 Leipzig, Germany (e-mail: lars-christian.horn@medizin.uni-leipzig.de).

M. Löffler is with the Institute for Medical Informatics, Statistics and Epidemiology, the Coordination Center for Clinical Trials, and the Interdisciplinary Center for Bioinformatics, University Leipzig, 04107 Leipzig, Germany (e-mail: markus.loeffler@imise.uni-leipzig.de).

Digital Object Identifier 10.1109/TMI.2005.855437

transmitted light microscopy once the tumor was surgically resected.

Among the microscopic techniques, apart from those with typically very limited fields of view (FOVs) and/or far sub-cellular spatial resolutions there is no well established 3-D procedure or protocol for tumor imaging providing appropriate contrasts/spatial ranges/resolutions. Therefore, we decided to do the data acquisition using conventional transmitted-light imaging based on HE-stained histological serial sections. The reasons for taking this modality are twofold: at this stage of our work we wanted to stay as close as possible to the procedure usually applied by the pathologist when assessing single slices in routine. Moreover, both the achievable spatial resolution (≈ 10 µm voxel edge length) and the effective FOV (typ. 0.1 cm^3) can be considered acceptable.

However, this necessarily requires solving the 3-D tissue reconstruction problem based on huge registered serial sections without having a reference data set available to co-register. On principle, this kind of problem has a long history and in fact was already tackled decades ago, e.g., in [9] and [10] proposing solutions using manually digitised line drawings. More recent work essentially could benefit from much improved computational power (especially concerning CPU and RAM) but also from (analogue, later digital) imaging improvements. Consequently, ambitious algorithmic solutions have been developed [11]–[13], partially treated as a co-registration problem [14]–[17]. Even though a completely different level of quality was reached meanwhile, due to its nature such 3-D reconstruction from serial sections remain complex and time-consuming. What is the central problem we are facing is the absence of some hard quality criterion to refer to. This means, we cannot utilize some reference data set since unfortunately there is none. This kind of dilemma has motivated us to strictly follow a coarse-to-fine strategy, i.e., we do the reconstruction in a stepwise manner and apply registration schemes with an increasing order of complexity, first a rigid one, then a polynomial nonlinear one, and finally a curvature-based nonlinear one.

The nine-criteria based classification of the required registration method(s) according to [18] would comprise: *2-D/2-D* (adjacent image pairs), *intrinsic-direct* (pixel/voxel property based only), *curved* (to compensate for nonlinear distortions, however, rigid registrations might be required in addition), *global* (affect entire images), *automatic* (no user interaction), with parameters obtained using an *optimization procedure* (even though procedures using explicitly computable parameters might be additionally applied), *monomodal* (histological sections only), *intra-subject* (no pair of data sets), and refers to *pelvic organs* (specimen of cervical tissue). What is crucial is the ill-posedness of the required underlying registrations [19], [20]. That means, registration results might be decisively affected from small changes in the images. And, for this work, some applicable algorithmic solution has to cope with a broad range of different tumor invasion patterns—without knowing their characteristics *a priori*. This paper introduces our newly developed dedicated processing chain. For an overview of the processing chain, see Fig. 4. It further elucidates quantitative results assessing the tumor growth based on 3-D data, and also discusses the above mentioned related work.

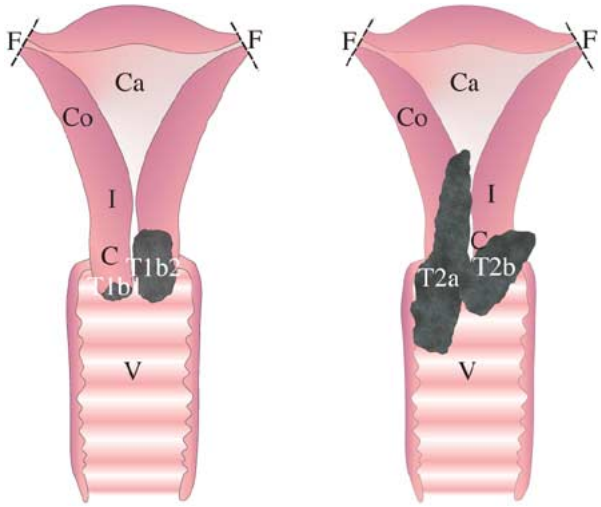

Fig. 1. Sketch of cut sections of the uterus depicting all tumor stages considered in this work. TNM nomenclature tumor stage T1b (see left) is defined as a lesion greater than a micro-invasive cancer, which has a microscopically measured invasion of stroma 5.0 mm or less in depth and no wider than 7.0 mm (as for T1a1 or T1a2), and as a tumor confined to cervix. Stage T1b is subdivided into tumors of 4.0 cm or less (T1b1) and more than 4.0 cm in size (T1b2). Stage T2 (see right) is defined as tumor invasion beyond the uterus but not to the pelvic wall or to the lower third of vagina. It is subdivided into cases without (T2a) and with (T2b) parametrial invasion. C: cervix uteri (neck of uterus), Co: corpus uteri (body of uterus), I: isthmus uteri (constricted part of the uterus between neck and body), Ca: cavum uteri (uterine cavity), F: openings of the uterine tubes (fallopian tube), V: vagina.

Main objective of this paper is to provide an automated algorithm objectively assessing the cervical tumor invasion based on 3-D reconstructed tissue volumes using serial sections of cervical specimen of resected uteri. Papers focussing on the histopathological and clinical outcome of this work are in preparation.

II. The Tissue Reconstruction Process

A. Tissue Samples and Digitization

This paper comprises an overall of thirteen specimens of squamous cell carcinoma of the uterine cervix (anatomic tumor stages T1b1, T1b2, T2a, and T2b, according to TNM nomenclature [7], [21], see Fig. 1), surgically managed by total mesometrial resection [22]. Three selected samples basically exemplify the different tumor invasion patterns observed in pathology routine (see Fig. 2).

The resected and formalin-fixed cervix was radially cut into specimens (thickness: 6–8 mm) which were paraffin-embedded (see Fig. 3), then serially sliced using a microtome HM355S by MICROM GmbH, Germany [Fig. 2(a): 500 @ 5 µm, Fig. 2(b): 100 @ 10 µm, Fig. 2(c): 230 @ 10 µm], and finally stained with hematoxylin-eosin (HE) using a staining machine. Sections as parallel planes starting from one of the radial cutting planes typically have a rough extent of 2.5 cm $\times$ 1.5 cm. The raw digitization area is 1300×1030 pixels corresponding to 10.45 mm $\times$ 8.28 mm $=$ 0.865 cm^2 at a nominal pixelsize of 8.04^2 μm^2. The digitization of the serial sections was carried out manually using the *AxioVision 3.1* controlling PC software directly reading from a digital 2/3″ one chip CCD-camera *AxioCam MRc* mounted on an *Axioskop 2 plus* transmitted light

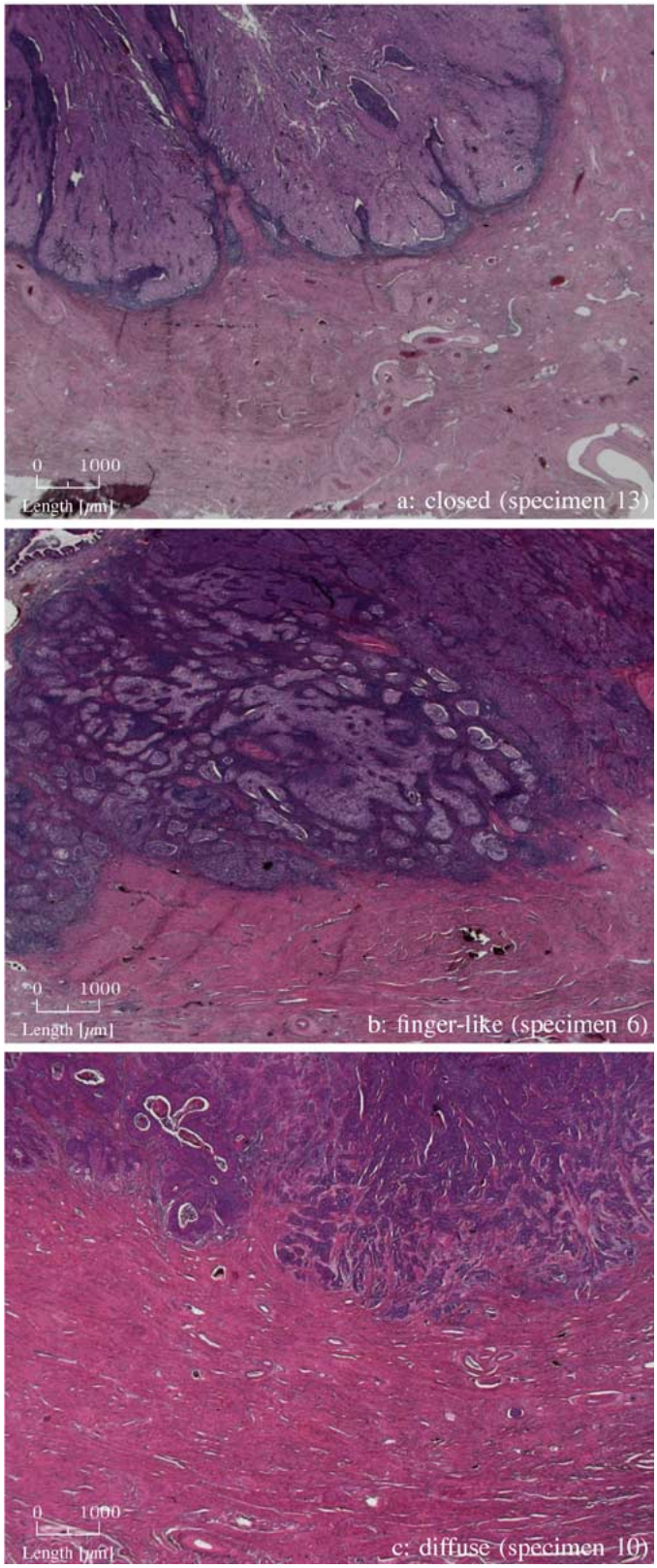

Fig. 2. Typical three-tiered verbal quantification of tumor invasion patterns based on single HE-stained slices.

microscope equipped with a *Plan-NEOFLUAR* 1.25 × objective and the *Video adapter 60C* 2/3″ 0.63 × (all mentioned products made by Carl Zeiss, AG, Germany).

Fig. 3. View onto a typical unstained cervix specimen embedded within paraffin ready for slicing on a microtome.

Under these conditions, due to the still limited FOV the digitization practically can be considered as a rough selection of a region of interest (ROI) within the tumor invasion front. Therefore, one also could refer to the placement of the microscope slides as a zero-order registration step in order to maximize the effectively reconstructible volume of interest (VOI) along the tumor invasion front.

Some fiducials would be difficult to apply in our framework. Since it remains unclear where the ROI/VOI within the specimen is located (without staining one cannot reasonably locate the tumor invasion front) one would need to have some stained reference section for "navigation." Then one would have to indirectly place some fiducials (e.g., four—one nearby each ROI corner). The choice of material is crucial (soft, but not too soft rods). However, we expect the drawbacks are greater than the benefits. Even if one would succeed placing the fiducials, one unavoidably introduces damages (direct, and also indirect, since the microtome blade could be much more worn). The benefit remains very limited, one could not spare any of the registrations which are detailed in the following.

B. Rigid Registration

In the first stage, a serial section undergoes a successive pairwise rigid co-registration of all slices. By this, the data set is restricted to an effectively captured VOI. The method is computed on scalar (gray-leveled) images obtained based on the luminance Y_{601} of the original RGB color images following the (old) International Telecommunication Union's recommendation ITU-R BT.601-5 as linear combination of the color primaries

$$Y_{601} = 0.299R + 0.587G + 0.114B. \tag{1}$$

The applied *AxioCam MRc* provides linear primaries (i.e., without gamma correction).

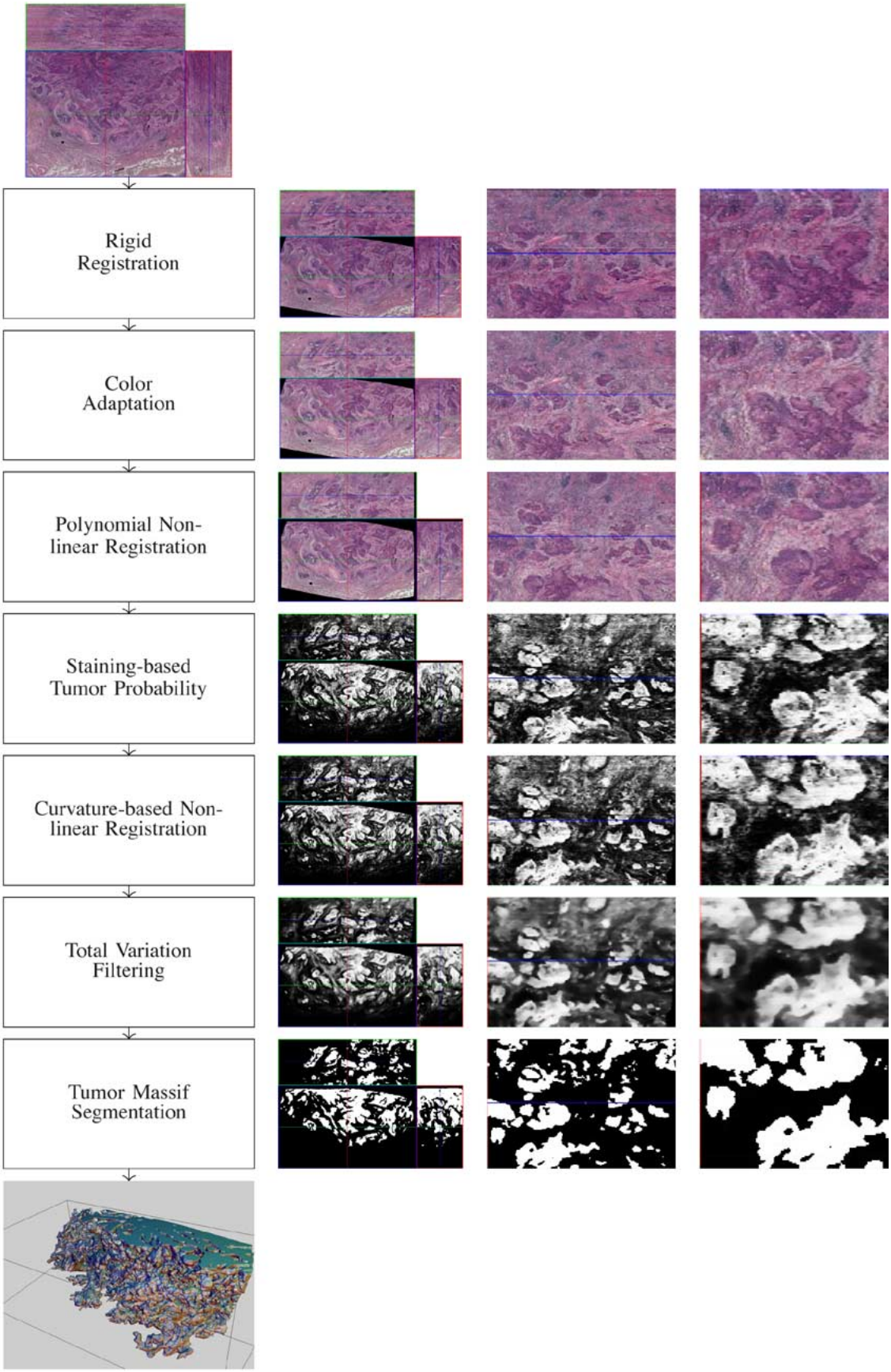

Fig. 4. An overview of the processing chain towards 3-D tumor invasion front reconstruction at the example of specimen 8. Just starting from the unregistered image stack, finally an appropriate basis for a subsequent automated 3-D invasion front quantification is provided. The second column consists of three orthogonal planes (two reconstructions: the x-z planes above and the y–z planes at right). In the third column, cutouts of the right half of the x–z planes (second column) are magnified, while in the fourth column even further zoomed cutouts are depicted (bottom-left quarters of the third column).

What has to be solved is the following transformation considering the parameters a_0 (rotation) and x_0, y_0 (translation) between the two scalar images $r(x,y)$ and $s(x,y)$

$$s(x,y) = r(x\cos\alpha_0 + y\sin\alpha_0 - x_0, \\ -x\sin\alpha_0 + y\cos\alpha_0 - y_0). \quad (2)$$

In fact, since s and r are images of adjacent sections, for the sake of simplicity in the notation any real existing differences of the images are neglected.

The approach we are using is a noniterative two-step algorithm consisting of a combination of the polar-logarithmic Fourier-Mellin invariant (FMI) descriptor, [23] and phase-only matched filtering (POMF) [24]. Variants thereof have successfully been applied in [25] and [26]. FMI basically is a polar-logarithmic transform accomplished on the Fourier transformed images converting both rotations and scalings into shifts. POMF is a matching technique representing an extension of the matched filtering approach. However, the latter is highly depending on the image energy rather than the spatial structures within. A solution, therefore, is to take a transfer function equal to the spectral phase as done by POMF. While the pure cross-correlation technique as, e.g., applied in [16], tends to result in quite broad/flat maxima, POMF will yield much narrower maxima. This method provides a reasonable compromise utilizing both energy and phase of the Fourier transformed images r and s. Experiments using a symmetric POMF as proposed as SPOMF in [25] resulted in even more narrow, sharper fits, however, with our histological data with a variety of slight damages (fissures, missing parts, folds) SPOMF turned out to be too susceptible compared with POMF.

The first part of the FMI-POMF-based scheme treats the rotational registration, while the second part takes this determined angle and computes the translation by means of another POMF. Hence, the goal of the very first step is to determine the angle α_0 by which the image $r(x,y)$ is rotated with respect to image $s(x,y)$

$$\begin{aligned} S(u,v) &= \mathcal{F}(s(x,y)) \\ &= \mathcal{F}(r(x\cos\alpha_0 + y\sin\alpha_0 - x_0, \\ &\qquad -x\sin\alpha_0 + y\cos\alpha_0 - y_0)) \\ &= \exp(-j\Phi_s(u,v)) \\ &\quad \cdot |R(u\cos\alpha_0 + v\sin\alpha_0, -u\sin\alpha_0 + v\cos\alpha_0)|. \end{aligned} \quad (3)$$

Herein, $\mathcal{F}$ denotes the Fourier transform and j the imaginary unit. While the spectral phase $\Phi_s(u,v)$ of the image $s(x,y)$ is closely depending on both translation and scaling, the spectral magnitude is translation invariant

$$|S(u,v)| = |R(u\cos\alpha_0 + v\sin\alpha_0, -u\sin\alpha_0 + v\cos\alpha_0)|. \quad (4)$$

Now, since what is of interest is a rotational angle, the spectral carthesian coordinates u and v are replaced by the spectral polar coordinates α (orientation) and ρ (wave number)

$$|S(\rho\cos\alpha, \rho\sin\alpha)| = |R(\rho\cos(\alpha - \alpha_0), \rho\sin(\alpha - \alpha_0))| \quad (5)$$

which is abbreviated in the following as:

$$s_{\mathrm{pol}}(\alpha,\rho) = r_{\mathrm{pol}}(\alpha - \alpha_0, \rho) \quad (6)$$

s_{pol} and r_{pol} are referred to as the FMIs of the images s and r, (2). By Fourier transforming (6) one obtains α_0 as phase shift

$$\begin{aligned} S_{\mathrm{pol}}(\nu,\omega) &= \mathcal{F}(s_{\mathrm{pol}}(\alpha,\rho)) \\ &= \exp(-j2\pi\nu\alpha_0)|\mathcal{F}(r_{\mathrm{pol}}(\alpha,\rho))| \\ &= \exp(-j2\pi\nu\alpha_0)|R_{\mathrm{pol}}(\nu,\omega)|. \end{aligned} \quad (7)$$

We determine this phase shift under the constraint that no scaling is assumed ($\rho = 0$) by the following POMF (the star * denotes the complex conjugate)

$$\alpha_0 = \arg\max_{(\alpha,\rho=0)} \left| \mathcal{F}^{-1}\left[\frac{\mathcal{F}(r_{\mathrm{pol}}(\alpha,\rho))}{|\mathcal{F}(r_{\mathrm{pol}}(\alpha,\rho))|} \cdot \mathcal{F}(s_{\mathrm{pol}}(\alpha,\rho))^* \right] \right|. \quad (8)$$

Finishing the first part, the intermediate result is

$$\tilde{r}(x,y) = r(x\cos\alpha_0 + y\sin\alpha_0, -x\sin\alpha_0 + y\cos\alpha_0). \quad (9)$$

For this part, the choice of the used rotational centre is arbitrary, however, since the images are naturally of limited extend, it is recommended to always take the physical centre of r in order to minimize boundary effects.

While the rotational part of the rigid registration is finished, the principle for solving the second part

$$s(x,y) = \tilde{r}(x - x_0, y - y_0) \quad (10)$$

is related

$$(x_0,y_0) = \arg\max_{(x,y)} \left| \mathcal{F}^{-1}\left[\frac{\mathcal{F}(\tilde{r}(x,y))}{|\mathcal{F}(\tilde{r}(x,y))|} \cdot \mathcal{F}(s(x,y))^* \right] \right|. \quad (11)$$

Now, applying (2) by inserting the results of (8) and (11) this rigid registration part is formally solved.

Further, for the implementation the following was applied.

- The images need to have an appropriate contrast. We take the following method for local contrast enhancement [27]

$$\hat{r}(x,y) = \kappa\frac{\mu_g}{\sigma_l}(r(x,y) - \mu_l) + \mu_l. \quad (12)$$

  Herein, μ_g and μ_l depict the global and local mean, respectively, while σ_l is the local standard deviation. "Local" refers to a squared vicinity centered around (x,y) with a side length of 55 which is about the maximum width of fissures in pixels. κ was set to 0.9 to obtain a strong but not maximum effect.
- The images should be windowed in order to reduce leakage artifacts of the fast Fourier transform (FFT) [28]. We used a Hann window

$$w(x,y) = \frac{1}{2}\left(1 - \cos\left(2\pi\frac{x}{N_x}\right)\right)\left(1 - \cos\left(2\pi\frac{y}{N_y}\right)\right). \quad (13)$$

  N_x and N_y are the image extents.

- For all re-sampling steps throughout this paper at least first order interpolation is recommended. We use higher order polynomial interpolation (cubic splines).
- In (5), only the half of the spectrum has to be considered, assuming that r and s are of real data, so that their Fourier transforms are mirror-symmetric w.r.t. u or v; the Hann window is, therefore, halved as well.
- The resolution of the angle α_0 depends on the implementation of (5); we take an angular scale of 720 for π resulting in a quarter-degree resolution; this does not imply any iterative angle search, (8) requires one single maximum search, where the index of the maximum is a direct measure for the angle.

Due to the applied FFTs, the time complexity of the rigid registration is $\mathcal{O}(n \log n)$ with n denoting the number of pixels, the memory complexity is $\mathcal{O}(n)$. For one image pair the algorithm runs about 1 s on a standard PC for image sizes around megapixels.

For an illustrative view on this processing step, for a typical slice-to-slice transition we have depicted the displacement vector field using line integral convolution [29], [30], see Fig. 5. This kind of visualization of directions and strenghs in vector fields is considered more illustrative than any direct plot of the vectors even though the respective sense of directions cannot be shown.

C. Color Adaptation

Once the first registration step is carried out, the effectively available tissue volume is more or less restricted to a core region depending on the accuracy of the slice placement during the digitization. Since the staining is going to have further importance for the tumor assessment, it is necessary to consider the achieved staining wrt. to its constancy. Even though applying a staining machine, the number of sections per series by far exceeds its capacity, so that series only can be stained by stages, thus unfortunately introducing fluctuations. Another reason for a similar effect are some very slight thickness variations which also can appear as fluctuations mainly affecting the color saturation.

This adaptation procedure is accomplished as second step, since the completely unregistered data set is inappropriate for doing a section-wise adaptation. Once the data has passed a first rough registration, for every section we can assume to have corresponding ROIs for all images which is not the case just after initial digitization. Hence, in this second step within the reconstruction procedure we are going to treat possible fluctuations of the staining along the serial sections. The idea behind the simple but effective procedure is as follows: the concerned sample image's staining is subsequently adapted using a linear color transform based on statistical distribution parameters.

So, the essence of the scheme we are proposing is just to force all sample images to have the same mean and covariance matrix applying a linear transform. In principle, what has to be computed is

$$\begin{pmatrix} \vec{M}_{s'}(x,y) \\ 1 \end{pmatrix} = \mathbf{T}(\vec{M}_r, \vec{M}_s) \begin{pmatrix} \vec{M}_s(x,y) \\ 1 \end{pmatrix} \qquad (14)$$

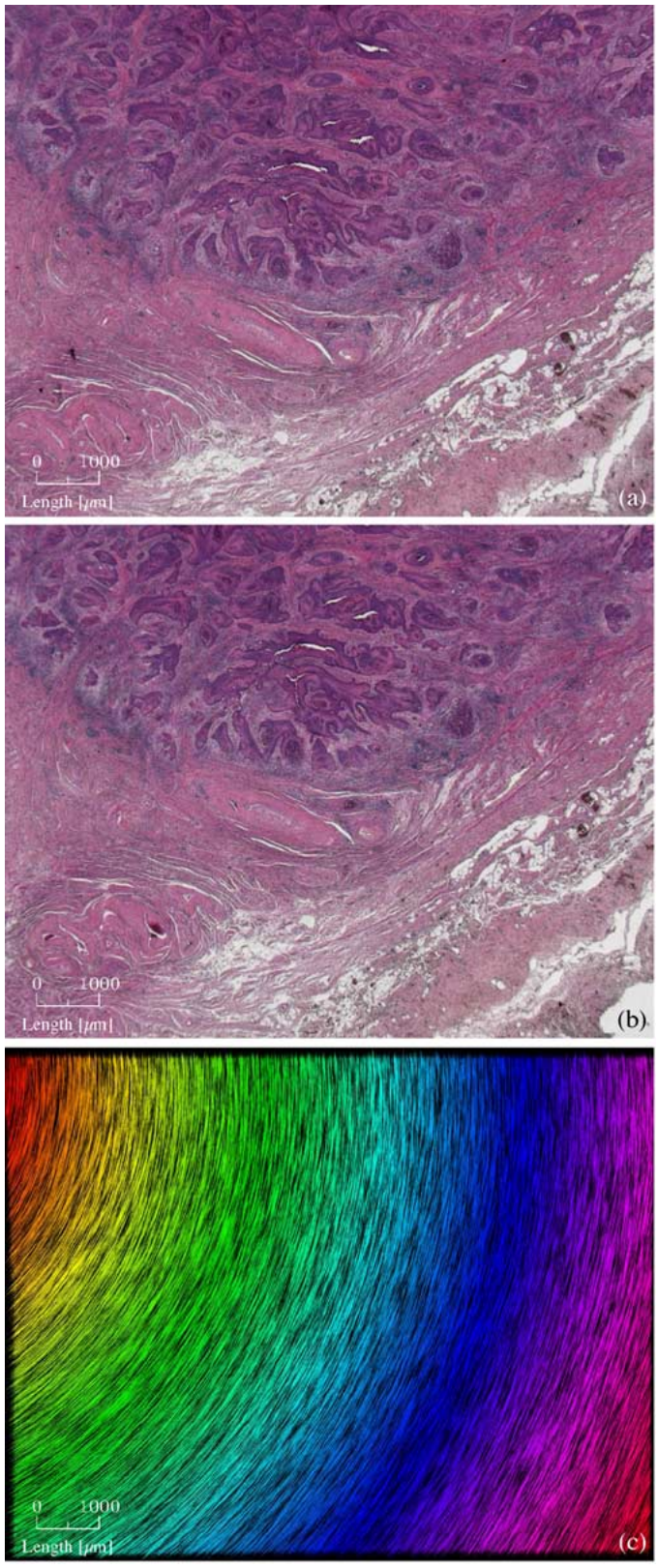

Fig. 5. Rigid registration examples: For a pair of adjacent slices (a) and (b) the displacement vector field to adapt (b) onto (a) according to the obtained parameters α_0, x_0 and y_0 is depicted using line integral convolution. The (cyclic) color codes the absolute value of the underlying displacements from purple-red (high) via blue, cyan, green, yellow to orange-red (low). The maximum displacement is 1184.3 µm (lower right), the minimum is 254.1 µm (upper left) which is located closely to the "rotational center" (outside the image).

(in homogeneous coordinates), where $\mathbf{T}$, $\vec{M}_s(x,y)$, $\vec{M}_{s'}(x,y)$, and $\vec{M}_r(x,y)$ denote the transform matrix, the sample section image, the transformed sample section image and the reference section image, respectively, while the latter is manually selected for each series.

$\mu_r = (R_m, G_m, B_m)$ where R_m, G_m, and B_m are the mean values of the red, green and blue image channel, respectively, on $\mathbb{K}_r$: We consider all $|\mathbb{K}_r|$ pixels belonging to the finite set $(x,y) \in \mathbb{K}_r$ only consisting of pixels with an intensity of at most 90% of the maximum intensity as well as with a minimum intensity above 0. This restricts the transform to nonbright image regions, since one can assume to have a background consisting of either bright or black image regions due to fissures or artificially filled black margins, respectively.

The transform $\mathbf{T}$ in (14) consists of the following matrix product:

$$\mathbf{T} = \mathbf{O}_r{}^{-1} \cdot \mathbf{R} \cdot \mathbf{S} \cdot \mathbf{O}_s. \tag{15}$$

Its individual factors are obtained as follows.

$\mathbf{O}_r$ and $\mathbf{O}_s$ denote the offsets (referring to $\vec{\mu}_r$ and $\vec{\mu}_s$, respectively) and are determined as

$$\mathbf{O}_r = \mathbf{I}_4 \cdot \begin{pmatrix} -\vec{\mu}_r \\ 1 \end{pmatrix} \tag{16}$$

and in analogy for $\mathbf{O}_s$, with $\mathbf{I}_4$ representing the identity matrix of rank 4.

$\mathbf{R}$ denotes the rotation matrix. It is obtained as matrix product

$$\mathbf{R} = \begin{pmatrix} & \mathbf{U}_r & & 0 \\ & & & 0 \\ & & & 0 \\ 0 & 0 & 0 & 1 \end{pmatrix} \cdot \begin{pmatrix} & \mathbf{U}_s{}^{-1} & & 0 \\ & & & 0 \\ & & & 0 \\ 0 & 0 & 0 & 1 \end{pmatrix} \tag{17}$$

wherein $\mathbf{U}_r = (\vec{u}_{1_r} \vec{u}_{2_r} \vec{u}_{3_r})$ is the matrix of sorted eigenvectors (wrt. decreasing order of their corresponding eigenvalues) of the covariance matrix $\mathbf{C}_r$ of the centered color value data (in analogy for $\mathbf{U}_s$ and $\mathbf{C}_s$)

$$\mathbf{C}_r = \frac{1}{|\mathbb{K}_r|} \sum_{(x,y) \in \mathbb{K}_r} \left(\vec{M}_r(x,y) - \vec{\mu}_r\right) \left(\vec{M}_r(x,y) - \vec{\mu}_r\right)^\top. \tag{18}$$

This real symmetric and orthonormal matrix and the mean vector represent an estimated multivariate distribution of the color values in RGB-space. Supposed $\mathbf{C}_r$ has the (full) rank 3, by solving the following eigenvalue problem:

$$(\mathbf{C}_r - \lambda_{k_r} \mathbf{I}_3) \vec{u}_{k_r} = 0 \tag{19}$$

one obtains the three eigenvalues λ_{k_r} and their corresponding eigenvectors $\vec{u}_{k_r}$. The problem was solved using Householder reduction to get a tridiagonal form and then based upon this using the QL algorithm (with implicit shifts).

$\mathbf{S}$ denotes the scalings along the principal axes, which are given as

$$\mathbf{S} = \begin{pmatrix} & \mathbf{U}_s & & 0 \\ & & & 0 \\ & & & 0 \\ 0 & 0 & 0 & 1 \end{pmatrix} \cdot \operatorname{diag}\left(\sqrt{\frac{\lambda_{r_1}}{\lambda_{s_1}}}, \sqrt{\frac{\lambda_{r_2}}{\lambda_{s_2}}}, \sqrt{\frac{\lambda_{r_3}}{\lambda_{s_3}}}, 1\right) \cdot \begin{pmatrix} & \mathbf{U}_s{}^{-1} & & 0 \\ & & & 0 \\ & & & 0 \\ 0 & 0 & 0 & 1 \end{pmatrix} \tag{20}$$

The time complexity of the color adaptation is $\mathcal{O}(n)$ with n denoting the number of pixels, the memory complexity is also $\mathcal{O}(n)$. For one image the algorithm runs less than 1 s on a standard PC for image sizes around megapixels.

Two examples are given in Fig. 6. Although the method is simple, the results can be considered adequate for our purposes since mainly staining-related outliers with small fluctuations are targeted. To the knowledge of the authors, even if simple, this method is not implemented in standard image manipulation software.

D. Polynomial Nonlinear Registration

This third stage basically does the compensation for slice-global distortions using polynomial warping [31] based on sparsely populated displacement vector fields taken from automatically determined control points. Its basic form is

$$\begin{aligned} t(x,y) &= s(a(x,y), b(x,y)) \\ &= s\Bigg(\sum_{i,j=0}^{N} p_{i(N+1)+j+1} x^j y^i, \\ &\qquad \sum_{i,j=0}^{N} q_{i(N+1)+j+1} x^j y^i\Bigg) \end{aligned} \tag{21}$$

while $t(x,y)$ represents an undistorted reference image and $s(x,y)$ the already rigidly registered but still distorted counterpart. The unknown coefficients $\vec{p} = (p_1, \ldots, p_{(N+1)^2})^\top$, and $\vec{q} = (q_1, \ldots, q_{(N+1)^2})^\top$ of the $2N$th degree polynomials (Nth degree for each independent variable) $a(x,y)$ and $b(x,y)$, respectively, can offhand be found once displacement vectors are available. Those displacement vectors rely on the pair-wise correlate of partially overlapping image tiles (i.e., subimages). These tiles are sized 128×128 pixels and overlap 96 pixels in both directions. 128 was taken as the most appropriate power of 2 (lots of FFTs have to be computed). The overlap results in a density of control points of one per 32 pixels which results in reasonable numbers of control points in the order of 1000. To prepare the tiling, we ensure the image dimensions to be multiples of the nonoverlapping tile size by adding an appropriate black margin. Again, we use POMF applied to all $m = 1, 2, \ldots, M$ tile pairs $s_m(x_m, y_m)$ and $r_m(x_m, y_m)$ for computing the correspondencies to the control points (x_m, y_m)

$$(x_{m_0}, y_{m_0}) = \arg \max_{(x_m, y_m)} \left| \mathcal{F}^{-1}\left[\frac{\mathcal{F}(r_m(x_m, y_m))}{|\mathcal{F}(r_m(x_m, y_m))|} \cdot \mathcal{F}(s_m(x_m, y_m))^* \right] \right|. \tag{22}$$

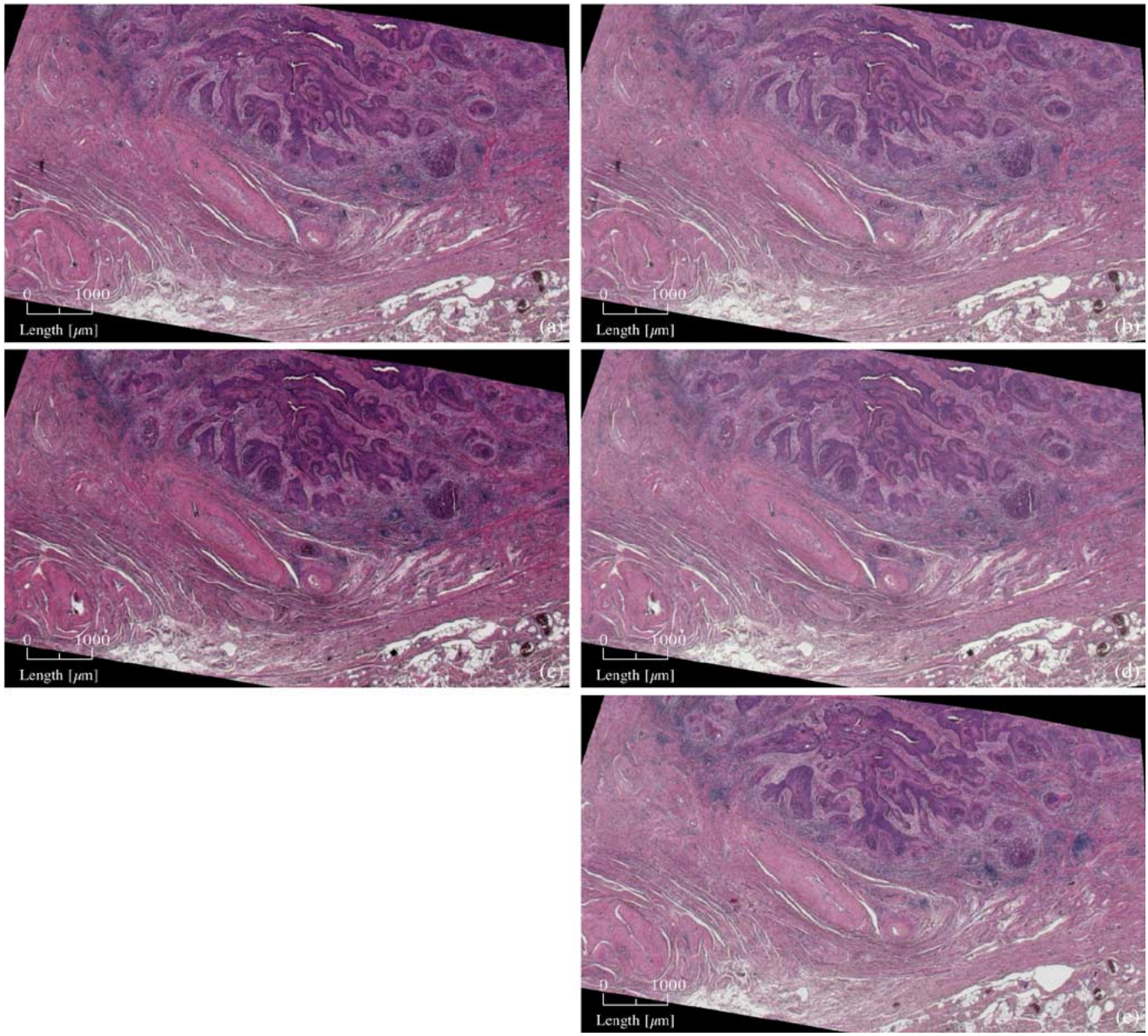

Fig. 6. Color adaptation examples: Usually the adaptation only leads to minor changes as from (a) to (b), whereas (a) is corresponding to Fig. 5(a) after rigid registration. In some cases, appearing as intensely stained as (c) a more obvious improvement can be achieved (d). Note that for this comparison (c/d) is not adjacent to (a/b), there was just one slice skipped in between in order to be more illustrative. The reference slice for this serial section is depicted in (e).

So, for a tile pair s_m and r_m the corresponding displacement vector is, e.g., $((x_m - x_{m_0}), (y_m - y_{m_0}))^\top$.

To get proper estimates of the coefficients $\vec{p} = (p_1, \ldots, p_{(N+1)^2})^\top$ and $\vec{q} = (q_1, \ldots, q_{(N+1)^2})^\top$ a multivariate linear regression using a least-squares (LS) error minimization is done. The multivariate model is

$$\mathbf{\Gamma} = \mathbf{U}\mathbf{\Psi} + \mathbf{\Xi} \tag{23}$$

with

$$\mathbf{\Gamma} = \left((x_{1_0}, \ldots, x_{M_0})^\top \quad (y_{1_0}, \ldots, y_{M_0})^\top \right) \tag{24}$$

representing the matrix of displacement vector end points and

$$\mathbf{\Psi} = (\vec{p} \quad \vec{q}) \tag{25}$$

an arranged matrix of all coefficients. For compactness reasons of the derivation, we have further introduced the matrix $\mathbf{U}$ referred to as design matrix which is build up from $M \cdot (N+1)^2$ products of combinations of the control point coordinates (i.e., the displacement vector start points)

$$\mathbf{U} = \begin{pmatrix} x_1^0 y_1^0 & x_1^1 y_1^0 & \cdots & x_1^N y_1^0 & x_1^0 y_1^1 & \cdots & x_1^N y_1^N \\ x_2^0 y_2^0 & x_2^1 y_2^0 & \cdots & x_2^N y_2^0 & x_2^0 y_2^1 & \cdots & x_2^N y_2^N \\ \vdots & \vdots & \ddots & \vdots & \vdots & \ddots & \vdots \\ x_M^0 y_M^0 & x_M^1 y_M^0 & \cdots & x_M^N y_M^0 & x_M^0 y_M^1 & \cdots & x_M^N y_M^N \end{pmatrix} \tag{26}$$

where $\mathbf{\Xi}$ is the error matrix in which the N^2+2N assumed pairwise linearly independent row vectors are supposed to represent

a 2-D multivariate normal distribution with an expectation value vector of $\vec{0}^\top$ as well as a covariance matrix $\mathbf{\Sigma}$.

The general form of the sum of squared errors is

$$S(\hat{\mathbf{\Psi}}) = \operatorname{trace}\left((\mathbf{\Gamma} - \mathbf{U}\hat{\mathbf{\Psi}})^\top(\mathbf{\Gamma} - \mathbf{U}\hat{\mathbf{\Psi}})\right) \tag{27}$$

which has to be minimized. $\hat{\mathbf{\Psi}}$ denotes an estimate of $\mathbf{\Psi}$. Now, differentiating (27) with respect to $\hat{\mathbf{\Psi}}$ and setting this expression zero in order to find an extremum one achieves

$$\begin{aligned}\frac{\partial S(\hat{\mathbf{\Psi}})}{\partial \hat{\mathbf{\Psi}}} &\stackrel{!}{=} 0 \\ &= -2\mathbf{U}^\top(\mathbf{\Gamma} - \mathbf{U}\hat{\mathbf{\Psi}}).\end{aligned} \tag{28}$$

Reforming (28), one easily can isolate $\hat{\mathbf{\Psi}}$ (supposed $\mathbf{U}$ has the full rank) and gets

$$\hat{\mathbf{\Psi}} = (\mathbf{U}^\top\mathbf{U})^{-1}\mathbf{U}^\top\mathbf{\Gamma}. \tag{29}$$

This solution is representing a minimum if the second derivative of (27)

$$\frac{\partial^2 S(\hat{\mathbf{\Psi}})}{\partial \hat{\mathbf{\Psi}} \partial \hat{\mathbf{\Psi}}^\top} = 2\mathbf{U}^\top\mathbf{U} \tag{30}$$

is positive definite which holds true if $\mathbf{U}$ has the full rank as already assumed above. Thus, the result of (29) can be considered valid. The two columns $\vec{\psi}_1$ und $\vec{\psi}_2$ of $\hat{\mathbf{\Psi}}$ are the estimates of $\vec{p}$ and $\vec{q}$, respectively, which now can be inserted in (21).

For the implementation of (29), even with a simple Gauß-elimination method and $N \leq 5$ no singularity problems throughout the matrix inversion have occurred. Unwanted warping effects as reported in [32] have occasionally occured, but could be managed as we have introduced the following extension: Supposed a number of $M = M_x \cdot M_y$ tiles (matching blocks) we artificially have added some $M_0 = 2(M_x + M_y + 1)$ control points (associated with zero-length displacement vectors) and placed them just along the image margin as a "frame" around the existing grid of control points. Under the condition that the rigid registration step was successful, this kind of "framing" is warrantable. This extension did decisively improve the method so that no "collapsing" or other unwanted warpings thereupon did occur. Further, differing to the previous rigid registration, this could be accomplished based on the luminance of the color adapted images.

The time complexity of the polynomial registration is $\mathcal{O}(n \log n)$ due to the FFTs with n denoting the number of pixels, the memory complexity is $\mathcal{O}(n)$. For one image pair the algorithm runs about 3 s on a standard PC for image sizes around megapixels.

Corresponding to Fig. 5 also for this polynomial registration step we give an illustration of the resulting displacement vector field for the same typical slice-to-slice transition, see Fig. 7 using line integral convolution.

E. Staining-Based Tumor Probability

Now, while two registration steps are done, the serial section is fairly re-aligned. Most of the slice-to-slice transitions can be considered smooth and misalignments appear mainly locally. To treat those remaining registration errors, we subsequently need to apply yet another registration step. Just like for the previous registration steps, this one also applies to scalar data. Despite of taking some luminance-related images, we, therefore, want to use scalar images highlighting the tumor regions. We generate such images simply by computing staining-based tumor probability maps relying on the HE staining applied to all slices short after sectioning. The probability maps are necessarily required for threshold-based tumor segmentation. The reason for swapping these two steps is mainly that by this we can further

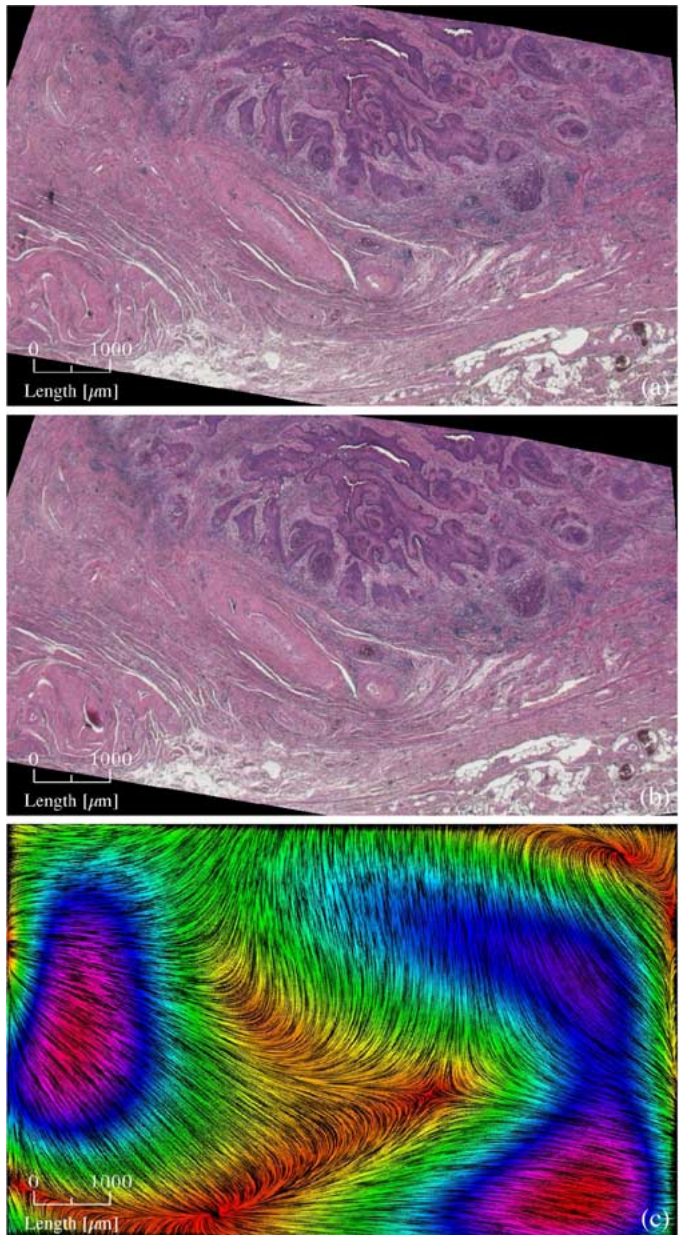

Fig. 7. Polynomial registration examples: Corresponding to Fig. 5, for a pair of adjacent images (a) and (b) according to the estimated polynomial coefficients the resulting displacement vector fields is visualised (c). The (cyclic) color codes the absolute value of the underlying displacements from purple-red (high) via blue, cyan, green, yellow to orange-red (low). The maximum displacement is 84.4 μm, the minimum is 0 μm. What is visible at the first glance is the inhomogeneity of the field, whereas on the right and left there are two distinct local maxima of the displacement, in this case the registrations leads to some contraction from the left/right/upper part toward a region around below the slice center. Two vortices (upper right and lower left) occur outside the physical slice and have very small strenghts.

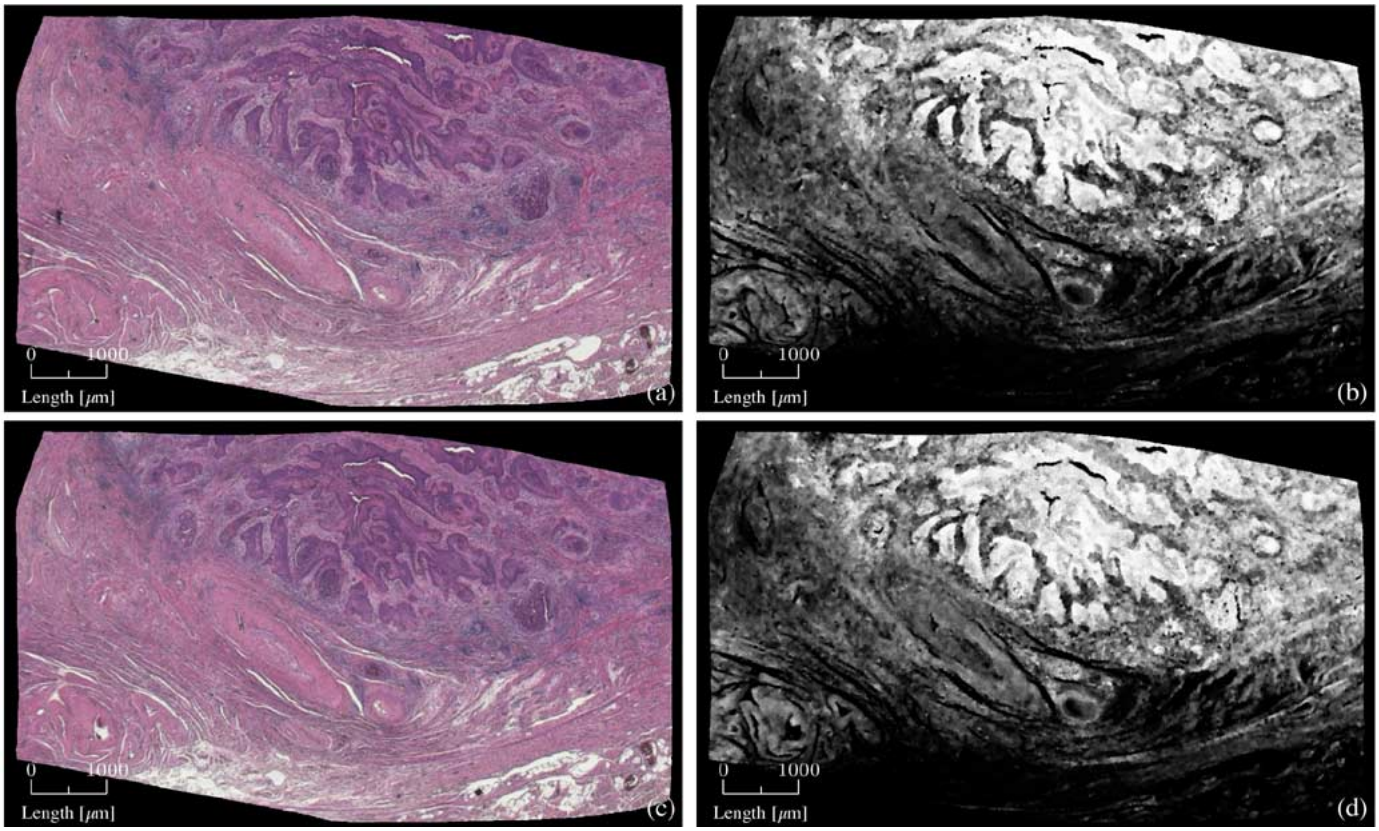

Fig. 8. Staining-based tumor probability computation examples: Corresponding to the image pairs of Fig. 6 we have taken the same two but now color corrected and polynomially registered images (a) and (c) and have determined the respective tumor probability maps (b) and (d). This example also illustrates the usefulness of the color correction by what the two probability maps appear qualitatively equal. Note that the suddenly emerging margin was artificially introduced in order to get image dimensions as multiples of primes up to 5 which is useful for the many FFTs accomplished in the following curvature registration.

attenuate artifacts mainly occurring outside the tumor regions, which facilitates the final registration step.

Basically, it is required to manually obtain representative tumor color samples from the respective serial section. Precisely, we arbitrarily select a number of ten slices equidistantly along the series and let the pathologist draw in the tumor boundary which provides us both with RGB color triple samples $(R,G,B)^\top$ for tumor and nontumor. Now, for the tumor probability we adopt normalized color values $(r,g,b)^\top = (R,G,B)^\top/\sqrt{R^2+G^2+B^2}$ leading to a projection onto a sphere sector fitting within the RGB cube, where $r^2+g^2+b^2 = 1$. One of the normalized components is redundant, so we can restrict to use $\vec{\xi} = (g,b)^\top$. We further assume that for the tumor c as well as for the nontumor m these components follow multivariate normal distributions. So, we estimate the multivariate densities for both sets

$$\rho_{c,m}(\vec{\xi}) = \frac{1}{\sqrt{(2\pi)^2|\mathbf{\Sigma}_{c,m}|}} \cdot \exp\left(-\frac{1}{2}(\vec{\xi}-\vec{\mu}_{c,m})^\top \mathbf{\Sigma}_{c,m}^{-1}(\vec{\xi}-\vec{\mu}_{c,m})\right) \quad (31)$$

with $\mathbf{\Sigma}_{c,m}$ and $\vec{\mu}_{c,m}$ denoting the covariance matrices and means, respectively. Finally, the probability for a pixel to exhibit the color of tumor at (x,y) is

$$\gamma(\vec{\xi}(x,y)) = \frac{\rho_c(\vec{\xi}(x,y))}{\rho_c(\vec{\xi}(x,y)) + \rho_m(\vec{\xi}(x,y))} \quad (32)$$

with $\gamma \in (0,1)$.

Fig. 8 illustrates the tumor probability computation for two images. The results indicate that the previous color-adaptation (compare Fig. 6) is justifiable.

The time complexity of the staining-based tumor probability computation is $\mathcal{O}(n)$ with n denoting the number of pixels, the memory complexity is $\mathcal{O}(n)$ as well. For one image the algorithm runs about 5 s on a standard PC for image sizes around megapixels.

F. Curvature-Based Nonlinear Registration

In this processing stage, remaining local registration errors are diminished and the image-to-image transitions are further smoothed. What generally has to be computed is a local displacement field as vector function $\{\vec{u}(\vec{r}) : \Omega \to \Omega\}$ with $\vec{r} = (x,y)^\top \in \Omega \subset \mathbb{R}^2$ considered as representation of the misalignments. The nonparametric procedure we are applying for this nonlinear registration uses a regularization term approximating local curvature, which was introduced in [33] and recently studied in [20], [34]. While the authors state that the algorithm would include an automatic rigid alignment, with our data we in fact could not benefit from this effect. This can be explained as follows: their images strictly cover some complete object(s) in front of a homogeneous background, so that it can be more or less assumed to successfully find *all* correspondences one-by-one. However, in our image material we do not have isolated objects with some delimited boundary. In fact, since the digitized regions usually do not comprise any background

but generally tissue, around the image margin for a considerable portion of the images pair-wise correspondences will be missing. Therefore, from the viewpoint of this algorithm the previous registration steps can be considered as preprocessing in order to drastically improve *a priori* image-to-image correspondence.

Basically, the distance measure to be minimized for this registration step is the sum of squared differences of the image's intensities [here, taken as tumor probabilities using (32)]. Again, assume $t(\vec{r})$ represents an undistorted reference image and $s(\vec{r})$ the already both rigidly as well as polynomially registered but still distorted counterpart, while the registration should do the mapping

$$t(\vec{r}) = s(\vec{r} - \vec{u}(\vec{r})). \tag{33}$$

With

$$\min_{\vec{u}} \left(D(\vec{u}) + \alpha S(\vec{u})\right) \tag{34}$$

we define a joint registration criterion consisting of the sum of squared differences

$$D(\vec{u}) = \frac{1}{2}\int_{\Omega} \left(s(\vec{r} - \vec{u}(\vec{r})) - t(\vec{r})\right)^2 d\vec{r} \tag{35}$$

and the smoothing term

$$S(\vec{u}) = \frac{1}{2}\sum_{i=1}^{2}\int_{\Omega} (\Delta u_i)^2 d\vec{r}. \tag{36}$$

From the calculus of variations we know that a function $\vec{u}$ minimizing (34) necessarily should be a solution for the Euler-Lagrange equation

$$\vec{f}(\vec{r}; \vec{u}(\vec{r})) - \alpha\Delta^2\vec{u}(\vec{r}) = 0 \tag{37}$$

with

$$\vec{f}(\vec{r}; \vec{u}(\vec{r})) = (s(\vec{r} - \vec{u}(\vec{r})) - t(\vec{r})) \cdot \nabla s(\vec{r} - \vec{u}(\vec{r})). \tag{38}$$

For the coupled system of 4th order partial differential equations [see (37)] an artificial time parameter t is introduced as

$$\frac{\partial \vec{u}}{\partial t}(\vec{r}, t) = -\alpha\Delta^2\vec{u}(\vec{r}, t) + \vec{f}(\vec{r}; \vec{u}(\vec{r}), t) \tag{39}$$

with the boundary condition of $\vec{u}$ being periodic across the image.

To solve (39) the time dependence is discretized using an implicit midpoint rule for the linear operator $L[\vec{u}](\vec{r}, t) = -\alpha\Delta^2 u(\vec{r}, t)$. For the integration over a single time step h one gets

$$\frac{\vec{u}^{(n+1)}(\vec{r}) - \vec{u}^{(n)}(\vec{r})}{h} = \frac{1}{2}\left[L[\vec{u}^{(n+1)}](\vec{r}) + L[\vec{u}^{(n)}](\vec{r})\right] + \vec{f}(\vec{r}, t; \vec{u}^{(n)}(\vec{r})) \tag{40}$$

for the propagation from $\vec{u}^{(n)}(\vec{r})$ to $\vec{u}^{(n+1)}(\vec{r})$. Defining the Green function

$$G[\vec{u}] = \left(1 - \frac{h}{2}L[\vec{u}]\right)^{-1}$$
$$G\left[1 - \frac{h}{2}L[\vec{u}]\right](\vec{r}) = \delta(\vec{r}) \tag{41}$$

the solution $\vec{u}^{(n+1)}(\vec{r})$ for the next time step is found by

$$\vec{u}^{(n+1)}(\vec{r}) = G\left[1 + \frac{h}{2}L[\vec{u}^{(n)}]\right](\vec{r}) + G[\vec{f}](\vec{r}; \vec{u}^{(n)}). \tag{42}$$

Denoting the discrete Fourier components

$$\mathcal{F}[\vec{u}]_{\mu,\nu} = \hat{\vec{u}}_{\mu,\nu} \tag{43}$$

and using [35, equation (25.3.33)] for the discrete version of the biharmonic operator, (42) in the Fourier domain is given by

$$\hat{\vec{u}}_{\mu,\nu}^{(n+1)} = \frac{24\left(h\hat{\vec{f}}_{\mu,\nu} + 2\hat{\vec{u}}_{\mu,\nu}^{(n)}\right)}{24 + \beta\gamma_{\mu,\nu}} - \hat{\vec{u}}_{\mu,\nu}^{(n)} \tag{44}$$

with

$$\begin{aligned}\gamma_{\mu,\nu} = {} & 368 + 160\cos(\mu\omega_\mu)\cos(\nu\omega_\nu) \\ & - 308\left[\cos(\mu\omega_\mu) + \cos(\nu\omega_\nu)\right] \\ & + 56\left[\cos(2\mu\omega_\mu) + \cos(2\nu\omega_\nu)\right] \\ & - 4\Big[\cos(3\mu\omega_\mu) + \cos(3\nu\omega_\nu) \\ & \quad + \cos(\mu\omega_\mu - 2\nu\omega_\nu) + \cos(2\mu\omega_\mu - \nu\omega_\nu) \\ & \quad + \cos(2\mu\omega_\mu + \nu\omega_\nu) + \cos(\mu\omega_\mu + 2\nu\omega_\nu)\Big]\end{aligned}$$

where $\beta = \alpha h/\delta^4$ and $\omega_\mu = 2\pi/M$ and $\omega_\nu = 2\pi/N$ for a $M \times N$ grid. When $\hat{\vec{u}}$ is computed the backward Fourier transform $\vec{u}$ is used to update $\vec{f}$. Every time integration step needs a total of four Fourier transforms for the two components of $\hat{\vec{u}}$ and the two components of $\vec{f}$. We have chosen periodic boundary conditions for the nonlinear registration. Other boundary conditions, e.g., with zero displacement on the boundary or zero normal derivative for $\vec{u}$ can also be used. It shoud be noted that we always could find a *single* transformation without the need of restarts.

Fig. 9 illustrates the curvature registration for an image pair using line integral convolution. Concerning the parametrization of the algorithm, for all specimen we have applied a fixed maximum number of 32 iteration steps, whereas α was set to 5.0 with an iteration time step h of 2.0. The solution is computed in the Fourier space. We have iterated some certain fix number of steps and applied both a fixed stepwidth and smoothing coefficient. Remember, reference-free registration is an ill-posed problem, so the difficulty is especially to avoid removing *all* differences between two adjacent sections/images. The specific choice of these mentioned parameters was made as follows: we

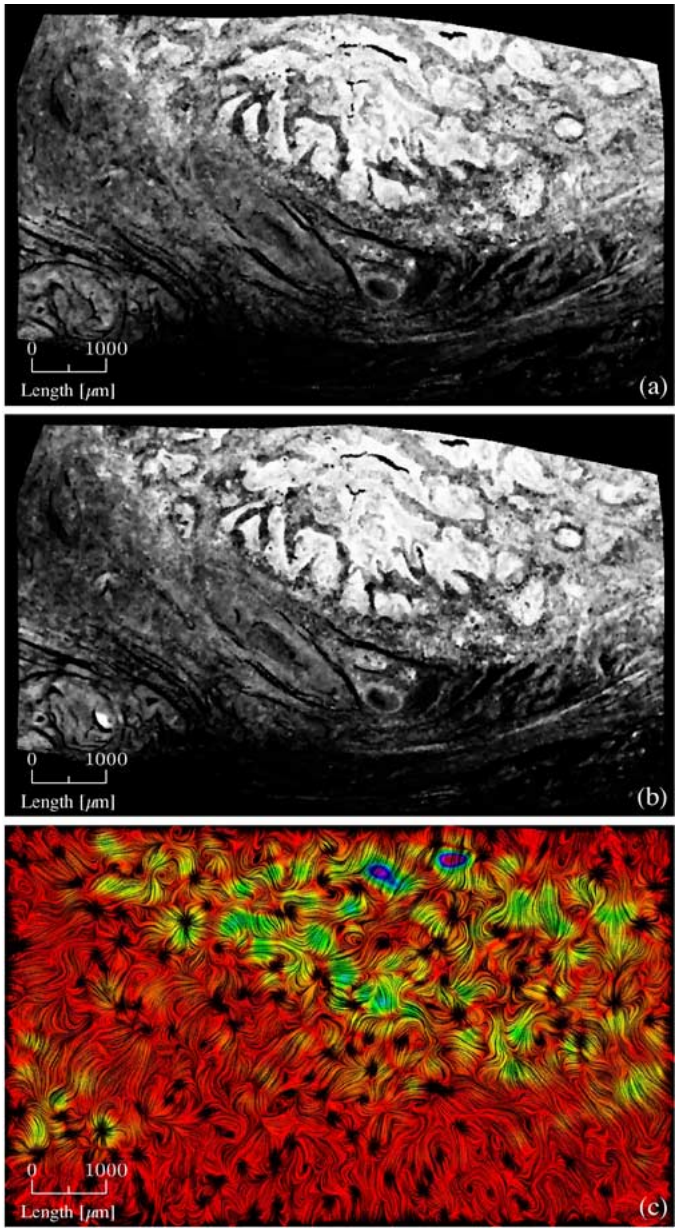

Fig. 9. Curvature-based nonlinear registration example: Corresponding to Figs. 5 and 7, for a pair of adjacent images (a) and (b) the determined displacement vector field is visualised (c) using line integral convolution. The (cyclic) color codes the absolute value of the underlying displacements from purple-red (high) via blue, cyan, green, yellow to orange-red (low). The maximum displacement is 36.2 μm, the minimum is 0 μm. Compared to Fig. 7 this displacement vector field is even more inhomogeneous and the displacements are at most half as far as for the polynomial step.

wanted to have the curvature term get weighted as five times as the squared differences. The time step and iteration steps were selected based on visual inspections of tests making sure that no eye-catching unwanted warpings occur. At the present stage of our work we did not implement any time dependency of these mentioned parameters.

To further improve the performance of those nonlinear schemes, [36], [37] have proposed algorithms what they have called *Pair-and-Smooth* registrations which combine geometric matching with intensity-based registration. This together with a multigrid implementation will be a future direction of our work.

Because of the FFT-based implementation, the time complexity of the curvature-based nonlinear registration step is $\mathcal{O}(n \log n)$, with n denoting the number of pixels, the memory complexity is $\mathcal{O}(n)$. For one image pair the algorithm runs about four minutes on a standard PC for image sizes around megapixels. Comparing this CPU time with the time necessary to do the microtome sectioning, the staining, the manual digitization, and a number of previous processing steps, we still consider some minutes acceptable for one image-to-image transition. With the above mentioned multigrid implementation (this is ongoing work) we expect a decisive computational speed-up.

G. Total Variation Filtering

Due to the pixel based color segmentation typically the data is affected by a significant amount of noise. While this noise is not essentially affecting the previous registration step, we consider the necessity for an intermediate processing on the reconstructed 3-D data step in order to facilitate the succeeding thresholding-based segmentation. Non-linear filters are in general much better in preserving image structures compared to linear ones. So, e.g., median filtering perfoming a ranking operation will keep edges but remove outliers while, on the other hand, linear binomial filtering will damp both. However, while the median filter [27] is appropriate in case of simple salt-and-pepper noise, its homogenizing properties remain limited. More sophisticated schemes like nonlinear diffusion filtering [38], [39] have been proposed, however these basically require some certain stopping criterion, otherwise the image structures get lost.

Instead, we have decided to apply nonlinear total variation filtering [40]. This filter minimizes the functional

$$\min_u \left(\int_\Omega |\nabla u(\vec{r})| d\vec{r} + \frac{\lambda}{2} \int_\Omega \left(u(\vec{r}) - u^{(0)}(\vec{r})\right)^2 d\vec{r} \right) \quad (45)$$

with $\vec{r} \in \Omega \subset \mathbb{R}^3$, for the scalar 3-D image $u(\vec{r})$ that contains the probability that at $\vec{r} = (x, y, z)^\top$ a cancer voxel can be found. Let $u^{(0)}(\vec{r})$ be the original noisy image with Gaussian white noise $\eta(\vec{r})$ exhibiting the following properties:

$$\begin{aligned} u^{(0)}(\vec{r}) &= u(\vec{r}) + \eta(\vec{r}) \\ E[\eta(\vec{r})] &= 0 \\ E[\eta^2(\vec{r})] &= \sigma^2. \end{aligned}$$

That $u(\vec{r})$ minimizing (45) generally can be obtained solving the Euler-Lagrange equation

$$0 = -\nabla \frac{\nabla u(\vec{r})}{|\nabla u(\vec{r})|} + \lambda (u(\vec{r}) - u^{(0)}(\vec{r})). \quad (46)$$

For this extremely nonlinear equation several solution methods are known. Since the considered volume data are very large, memory intensive methods are not feasible, because a nonlinear solver would require several gigabytes of temporary memory.

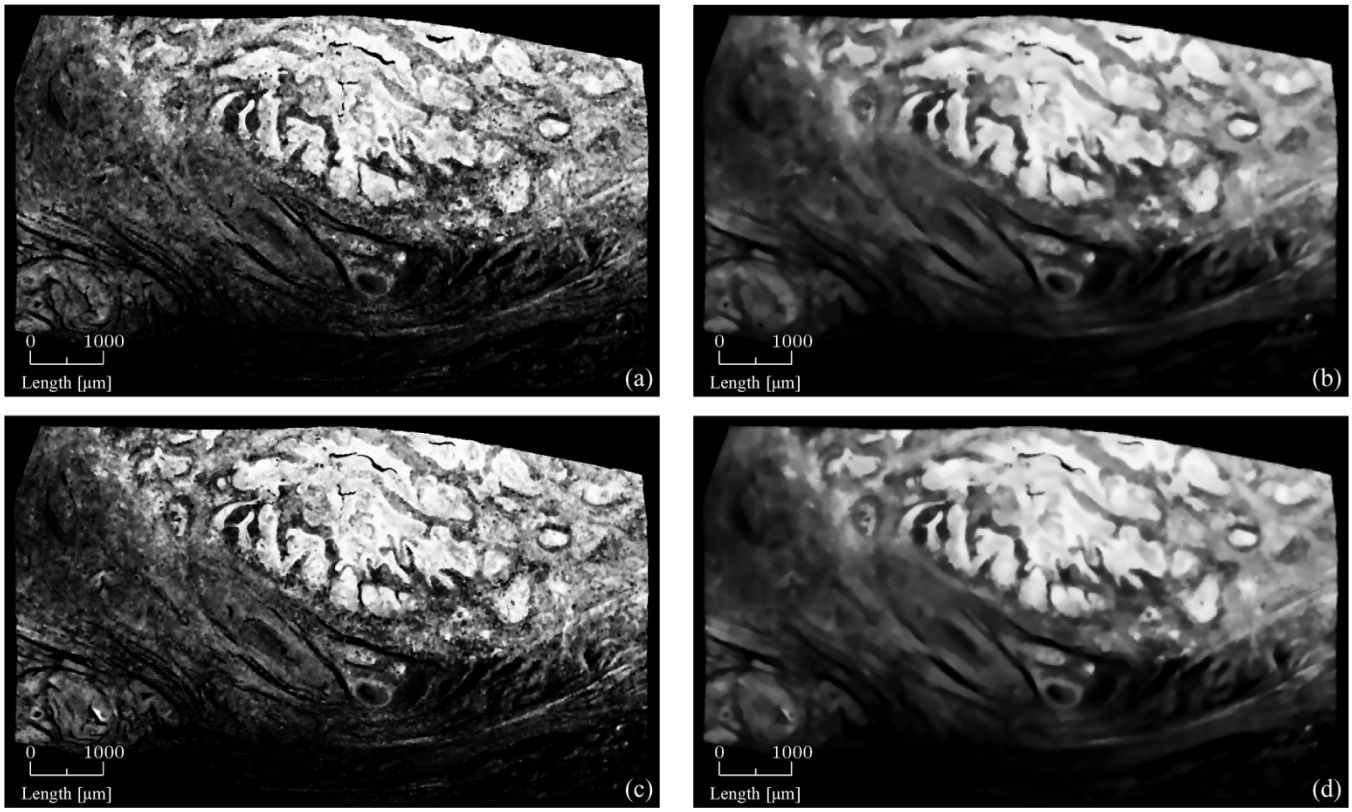

Fig. 10. Total variation filtering examples: This example again refers to the same pair as in Fig. 9. The two images of the adjacent slices (a) and (c) were transformed by the curvature-registration, and now were TV filtered attaining an edge-preserving smoothing as depicted in (b) and (d). Note that the TV filtering is applied as 3-D operation, which is why we show this adjacent pair here (the 3-D effect can be best seen in the nontumour background).

However, an appropriate solution method with low memory demands was proposed by Osher et. al. [40]. It transforms the problem into a time dependent problem for $u(\vec{r},t)$ with $u(\vec{r}) = \lim_{t\to\infty} u(\vec{r},t)$. So, instead of (46) we apply

$$\frac{\partial u}{\partial t}(\vec{r},t) = \nabla\frac{\nabla u(\vec{r},t)}{|\nabla u(\vec{r},t)|} + \lambda(u^{(0)}(\vec{r}) - u(\vec{r},t)) \tag{47}$$

with $\{u : \Omega \times \mathbb{R} \to \mathbb{R}\}$. In regions where the gradient vanishes, the equation becomes singular so that the gradient must be regularized as

$$|\nabla u|_\alpha = \sqrt{|\nabla u|^2 + \alpha^2} \tag{48}$$

$$= \sqrt{(\partial_{x_1} u)^2 + (\partial_{x_2} u)^2 + \cdots (\partial_{x_n} u)^2 + \alpha^2} \tag{49}$$

considering $0 < |\alpha| \ll 1$. For the discrete solution

$$|\nabla_a u|_\alpha = \sqrt{\sum_{\langle a,b\rangle} (u_a - u_b)^2 + \alpha^2} \tag{50}$$

the summation runs over all next neighbors of a which is denoted as $\langle a,b\rangle$. For inner points in the volume a 6-neighborhood stencil is used. Boundary points cover a reduced neighborhood as respective grid points exist. This yields a nonlinear filter for every mesh point a

$$u_a{}^{(n+1)} = \sum_{\langle a,b\rangle} h_{a,b}(u)u_b + h_{a,a}(u)u_a{}^{(0)} \tag{51}$$

with

$$h_{a,b}(u) = \frac{w_{a,b}(u)}{\lambda + \sum_{\langle a,c\rangle} w_{a,c}(u)}$$

$$h_{a,a}(u) = \frac{\lambda}{\lambda + \sum_{\langle a,c\rangle} w_{a,c}(u)}$$

and

$$w_{a,b}(u) = \frac{1}{|\nabla_a u|_\alpha} + \frac{1}{|\nabla_b u|_\alpha}.$$

This filter acts as an edge preserving low pass. During the calculation one simultaneously needs to store at least three data sets $u^{(0)}$, $u^{(n)}$ and $u^{(n+1)}$. The main advantage of the filter is its relatively quick convergence toward the denoised result. The only free parameter is λ. Its choice is of importance for the denoising quality. Following [40] we use

$$\lambda = \frac{1}{\sigma^2}\frac{1}{|\Omega|}\sum_a \sum_{\langle a,b\rangle} w_{a,b}(u_b - u_a)(u_a{}^{(n)} - u_a{}^{(0)}) \tag{52}$$

with the standard deviation of the white noise σ^2 and the number of mesh points $|\Omega|$. After 5–10 iterations a new λ is computed and used for the update of the $u^{(n+1)}$.

The time complexity of the total variation filtering is $\mathcal{O}(n)$ with n denoting the number of voxels, and also the memory complexity is $\mathcal{O}(n)$. For one image series with typically 300 sections the algorithm runs about half an hour on a standard PC for image sizes around megapixels. This step is a 3-D operation, so it may have exorbitant RAM requirements, since $u^{(0)}$, $u^{(n)}$ and $u^{(n+1)}$ have to be accessible simultaneously.

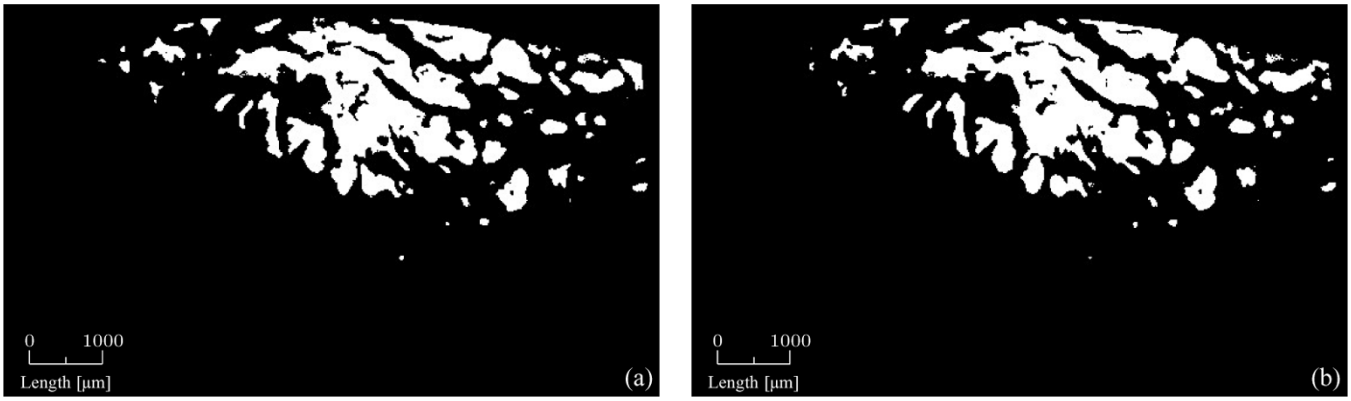

Fig. 11. Tumor segmentation example: The two images (a) and (b) show the results after thresholding the TV filtered images in Fig. 10(b) and (d), respectively

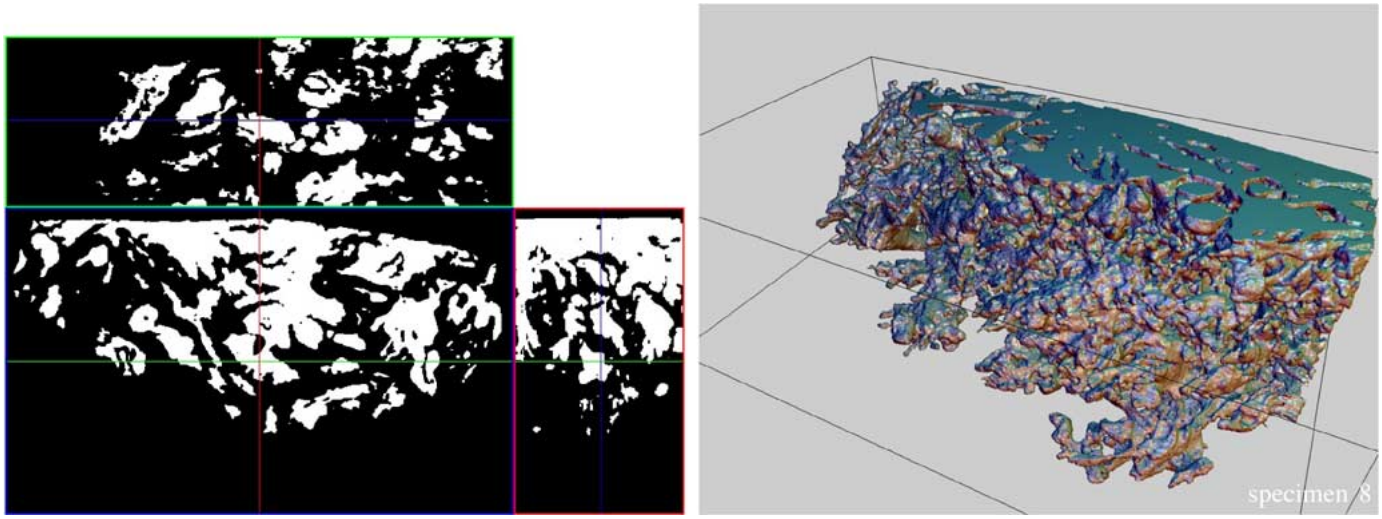

Fig. 12. (left) Multiplanar reconstruction and (right) 3-D surface rendering of the invasion front for specimen 8.

Fig. 10 illustrates the 3-D TV filtering effect on a pair of adjacent images.

H. Tumor Segmentation

In this final reconstruction step, just the TV filtered volume data is binarized. According to (32) an illustrative criterion for thresholding is where the two estimated densities for tumor and nontumor exhibit the same magnitude so that the tumor probability is 0.5. Let $s(\vec{r})$ represent the previously TV filtered scalar image, the binarized result $t(\vec{r})$ is obtained as

$$t(\vec{r}) = \begin{cases} 1, & \text{for } s(\vec{r}) \geq 0.5 \\ 0 & \text{for } s(\vec{r}) < 0.5. \end{cases} \tag{53}$$

Both time and memory complexity of thresholding of course is $\mathcal{O}(n)$ with n denoting the number of voxels. It takes a fraction of 1 s on standard PC hardware.

Fig. 11 gives examples corresponding to the results of Fig. 10.

III. Invasion Front Quantification

Once the smoothing by means of total variation filtering and the segmentation was accomplished, following the 3-D reconstruction process the tumor invasion front within the volume data is going to be assessed. Hence, the invasion front firstly is visualized and subsequently quantified.

A. Three-Dimensional Tumor Visualization

What is of basic interest is the topology of the invasion front. One of the interesting questions at hand is how the tumor invasion front is shaped. Another question is the presence of possibly separated tumor islets apart from the main tumor. Some virtually have occured but turned out to have direct contact to the data set outskirt. These were sorted out since it cannot be decided if separated or not. The rest, however, was not straightforward to be verified or falsified, due to the limitations of the HE staining. HE in fact is just enhancing image contrast with respect to the averaged local cell kernel density. In tumor cells, the kernels are basically enlarged. In exceptional cases, misclassifications might occur as, e.g., for smaller inflamational cells or some other dense tissue parts. We have let the pathologist check all suspected tumor islets using a much larger magnification ($40\times$ instead of $1.25\times$) but got none of them verified to consist of tumor. What has remained for all our specimen was one large connected tumor segment, a kind of "massif" VOI of the tumor invasion front.

Therefore, in order to give a 3-D illustration of the reconstructed tumor invasion, we do a surface rendering applying the

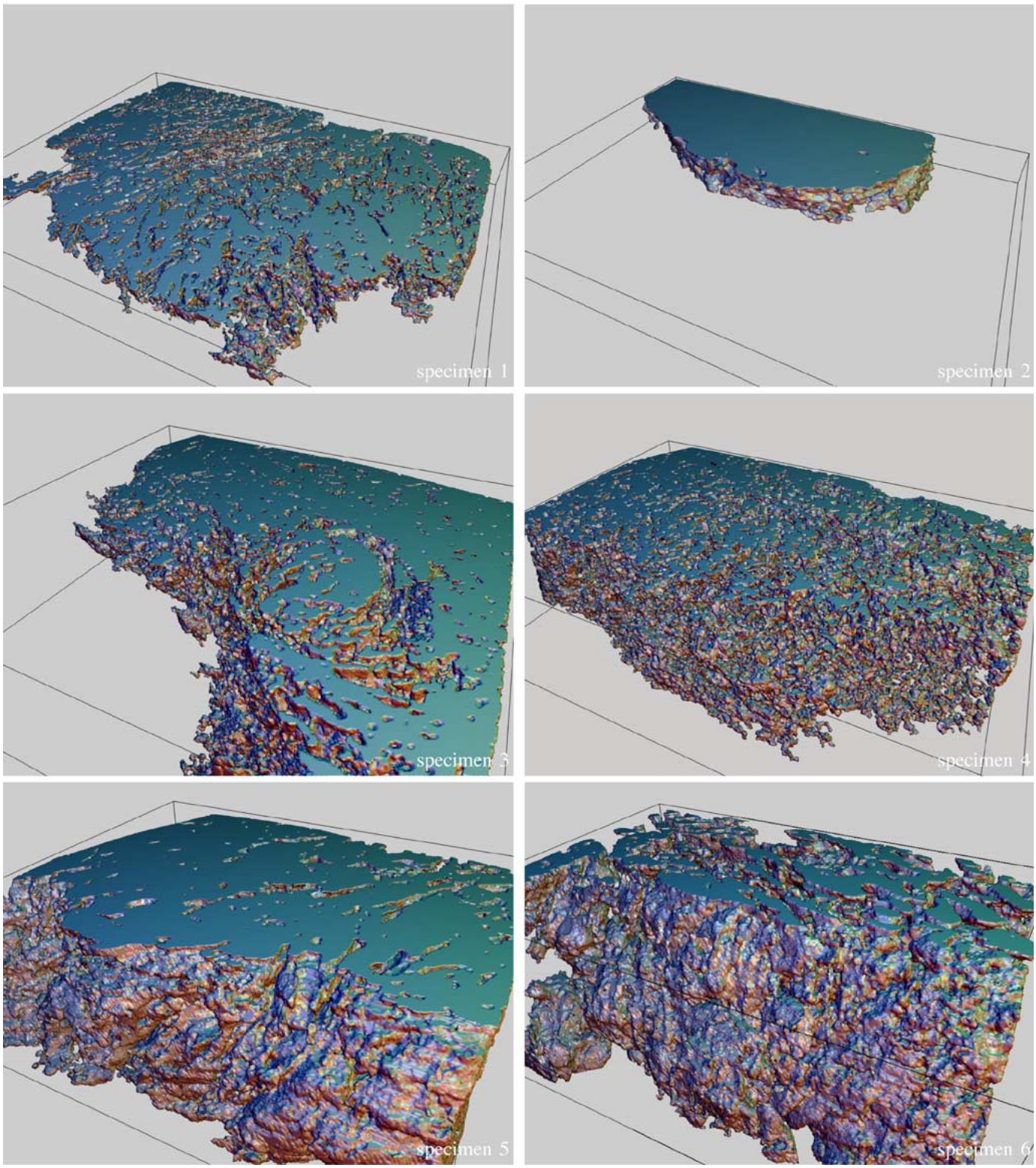

Fig. 13. Views onto the 3-D surface renderings of tumor invasion fronts, part I.

thresholding criterion from (53). The rendering of the tumor surfaces uses the well-known algorithm from [41] with the mesh displacement modification [42], [43]. A detailed discussion of rendering algorithms can be found in [44].

The gallery of tumor invasions of our 13 specimens is shown in the Figs. 12–14. These are the first-ever visualizations of a solid tumor's invasion front with a resolution of $\approx$ 10 μm. The renderings have been generated using MathGL3d [45], an OpenGL-based interactive viewer for Mathematica's 3-D graphics. Typical numbers of (potentially nonconnected) surface polygons occur from $1, \ldots, 5 \cdot 10^6$. For a typical image series with 300 sections and image sizes around megapixels

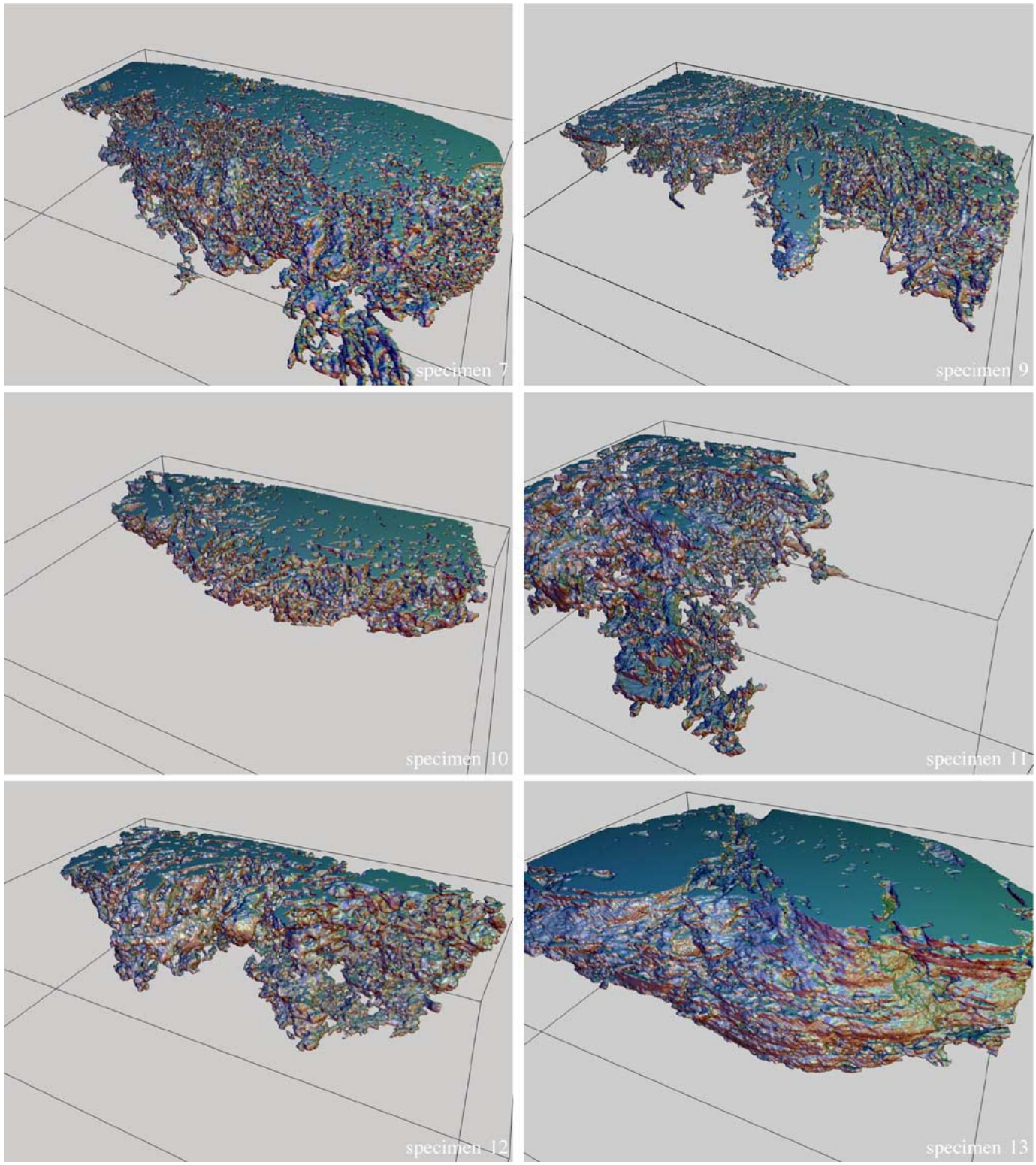

Fig. 14. Views onto the 3-D surface renderings of tumor invasion fronts, part II.

the algorithm runs about 5 min on a standard PC with OpenGL graphics hardware, but of course this will closely depend on the respective invasion front morphology.

B. Invasion Quantification

Another highly important goal of this paper is to give a quantitative characterization of the 3-D reconstructed invasion front. Just doing a verbal assessment of the invasion obviously is not really satisfactory. Contrary to the common constellation, we do not want to provide something closely mimicking the pathologist's assessments, e.g., as in cytology. Just conversely, the pathologist is lacking some reproducible quantitative means. As recently pointed out in a review on the parameters of prognosis in cervical cancer by Singh and Arif [46], there is too much

confusion in the assessments of the importance of the invasion pattern: "The importance of pattern of invasion as an independent prognostic factor is extremely difficult to evaluate due to varying definitions and parameters." Obviously, this clear statement is articulating the relevance of our work.

In principle, there are a couple of possibilities feasible for quantification, e.g., descriptions with components basically consisting of tumor surface areas or volumes, or differential-geometric properties. However, considering fractal properties would basically suffer from far too small tumor/VOI size to cell diameter ratios rather than being primarily a problem of digitization resolution. At most, four orders of magnitude are not considered to be sufficient for reliably analyzing some supposed self-similarity.

Alternatively, more feasible and even more promising should be a description relying on the sizes of both tumor surface and volume. A pretty much known description consisting of just these two components is *compactness*. This is an intrinsic 3-D object property and is dimensionless defined as $\text{surface}^3/\text{volume}^2$ with the sphere as that object providing the absolute minimum at 36π. Direct compactness implementations, however, do lack of sufficient robustness i.e., surface enlargements due to noise could lead to the same compactnesses like real surface shape changes. A new way to determine a compactness which far less can be irritated is *discrete compactness* C_D introduced in [47]. Instead of directly considering surface and volume, C_D relies to internal voxel contact surfaces and is defined simply as

$$C_D = \frac{A_C - A_{C_{\min}}}{A_{C_{\max}} - A_{C_{\min}}}. \tag{54}$$

Herein, A_C denotes the number of voxel contact surfaces within a 3-D object consisting of $n \geq 2$, $n \in \mathbb{N}$ voxels, whereas correspondingly $A_{C_{\max}} = 3(n - n^{(2/3)})$ is the theoretical maximum of contact surfaces achieved with a cubic object also consisting of n voxels (isotropic case). Contrasting to [47], we define $A_{C_{\min}} = 0$, in order to consistently allow for objects consisting of neighboring voxels even without contact surfaces, so that $C_{D_{\max}} = 1$ for a "cube" and $C_{D_{\min}} = 0$ for a diagonal "voxel chain." A sphere, however, build up from discrete voxels, obviously would be evaluated little less compact than a cube.

The time complexity of the compactness computation is $\mathcal{O}(n)$ with n denoting the number of overall tumor voxels, the memory complexity is again $\mathcal{O}(n)$. For one image series with typically 300 sections the algorithm runs several seconds on a standard PC for image sizes around megapixels.

IV. Experiments

So far, the processing chain meanwhile was applied to an overall of 13 specimens of squamos cell carcinoma of the uterine cervix. No special selection criterion was applied except the tumor stage to be within T1b1 and T2b. Despite utmost care due to unavoidable but inacceptable damages, e.g., large folds and/or fissures up to 2% of the sections had to be sorted out, those were replaced by adjacent sections.

The overview given in Fig. 4 is intended to illustratively exemplify how the histological image data is effected for each processing step. The three-plane orthogonal reconstructions (all planes intersect at the center of the cuboid) each with two reconstructed images may illustrate how the tumor segment boundaries are getting smoother. It should be noted, however, that de-

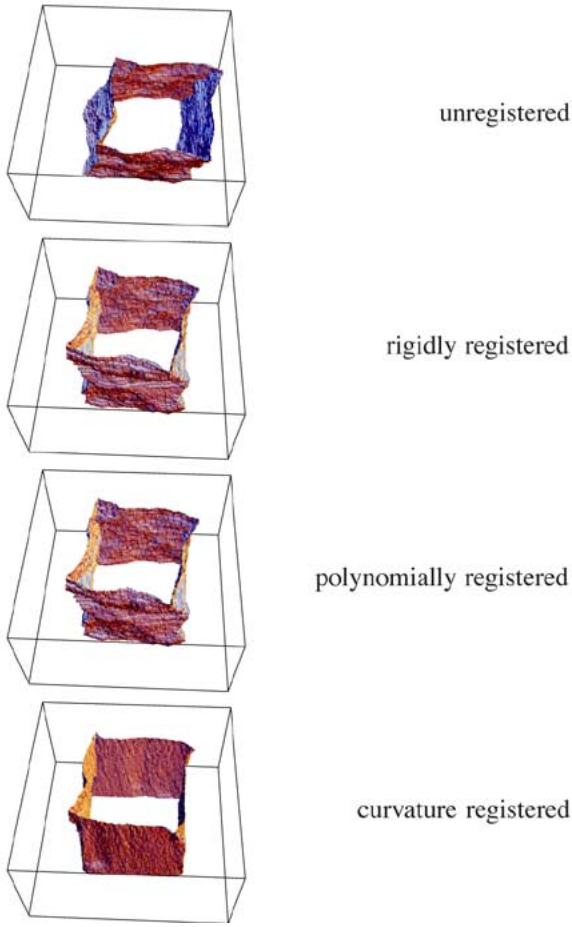

Fig. 15. The three registration steps applied on synthetic data: The binary cuboid object consisting of a sequence of 33 artificial 256×256 slices which underwent some disturbance consisting of a shift, a rotation, and finally a superimposition with Perlin noise. The three registration steps can restore the original cuboid (not shown) quite good. Note that in each case the registrations were accomplished from bottom toward the top of the "stack" of slices. The outcomes of the rigidly registered and the polynomial step do not differ that much for this test case. This is since the underlying control point related displacement vectors are predominantly zero for the polynomial registration due to the binary data.

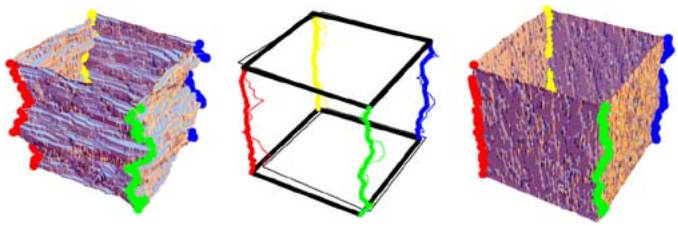

Fig. 16. This figure demonstrates the preservation of the corners for another synthetic data set with 33 distorted squares when registering using the curvature-based method alone. The left figure shows the outline of the stack of unregistered images and the position of the corners labeled as red, green, blue and yellow points. The right image shows the outline after the curvature registration as well as the corresponding transformed corners. The superimposition in the middle shows the path of the corner points along the z-direction before (thin lines) and after the registration (thick lines) as well as the connecting straight lines for the corners in the upmost and lowest image plane. The registration was done with $\alpha = 5$ and $h = 5.5$ over not more than 1024 steps for every image along the stack.

TABLE I
DETAILS OF SERIAL SECTION PROPERTIES, REGISTRATION QUALITY ASSESSMENTS AND INVASION QUANTIFICATION

No.	Number of Slices	Slice Thickness [μm]	Reconstructed Volume [mm^3]	Mean Residual Deviation [μm]			Verbal Assessment	Tumor Stage	Compactness
				Rigid Reg.	Polynomial Reg.	Curvature Reg.			
1	96	10	60.2	20.1	12.9	5.9 (9.6)	diffuse	T2a	0.884
2	90	6	16.7	13.2	7.5	7.1 (12.9)	closed	T2b	0.995
3	230	10	146.1	15.7	7.8	5.6 (11.5)	diffuse	T2b	0.954
4	230	10	133.6	12.9	5.9	3.5 (6.6)	finger-like	T1b1	0.915
5	250	10	130.8	10.7	9.8	6.2 (6.8)	closed	T1b1	0.966
6	300	10	104.7	10.9	7.0	3.9 (5.4)	finger-like	T1b1	0.935
7	250	10	148.9	14.7	7.7	4.8 (9.0)	diffuse	T1b1	0.906
8	300	10	146.8	10.6	5.9	3.5 (6.3)	finger-like	T2b	0.951
9	150	10	100.5	15.9	8.6	5.0 (8.7)	diffuse	T1b2	0.881
10	100	10	62.8	14.1	7.5	5.2 (10.4)	diffuse	T1b1	0.944
11	301	10	143.4	11.5	8.0	5.9 (9.2)	diffuse	T2b	0.892
12	260	10	123.8	15.2	10.3	7.5 (11.7)	finger-like	T1b1	0.902
13	500	5	89.3	13.0	7.5	5.1 (9.1)	closed	T1b1	0.976

spite the nominal plane coordinates remain fixed, the progress cannot be assessed by strict one-by-one comparisons, since each registration just might correct for some *a priori* unknown remaining trend.

Due to this kind of difficulties in assessing especially the three registration steps, we have accomplished some experiment with synthetic data shown in Fig. 15. For a binary cuboid object the zeroth (artificial) slice remained an undistorted square (128×128 pixels, not depicted) while all following 33 slices underwent a progressive change consisting of a shift, a rotation, and finally a deformation using a Perlin noise superimposition. So we gained some special but difficult case where the deformation is quasi-continuous along the stack. What is visible is that after the polynomial registration there is almost no improvement compared to the preceding rigid registration. The reason is that for this binary object too few nonzero length displacement vectors can be obtained. The curvature registration in turn, which operates more locally and is applied iteratively, computes a complete displacement vector field and by this is quite satisfactorily reconstructing the cuboid shape. Differing to the procedure on real data, we have largely extended the number of iteration steps which was set to 256. There is no doubt that for our real data this kind of smoothness is not adequate. While for our example our goal was to demonstrate to what degree the curvature registration can be operated, we deliberately take a much lower number of steps, i.e., our choice with 32 steps is considered to be quite conservative and will decisively reduce unwanted warping.

Some important aspect is documented in Fig. 16. In this second example, we focus on the consistency of the curvature registration. We demonstrate this with respect to the corners of the synthetic images before and after the processing for the whole stack. It becomes visible that even for this most flexible nonlinear registration corners remain just corners and no unwanted warping occurs. For the other two registrations such warping is not really an issue. While impossible for the rigid step, this is also no serious problem for the polynomial step. The latter basically can degenerate, but by this the transformation would completely corrupt the image. We actually did not observe such corruptions using polynomials with degrees up to five.

To illustrate the basic effects of the registration steps on real data we would again like to refer back to the line integral convolutions in Figs. 5(c), 7(c), and 9(c). Note that in these images the length of the displacement field lines are not exhibiting the respective displacements but just the course of the field. Instead, the length is color coded (with each example using an own, adapted scale). Both displacement lengths as well as the courses of the displacements exemplify each step's main focus: the general movement to roughly align the pair, the slice-global dewarping, and the local nonlinear adjustments, respectively.

Concerning whole serial sections, several quantitative details on the 13 data sets are given in Table I. For the three respective registration steps, mean residual registration deviations are given. For a serial section with N slices, for each of the $N-1$ adjacent pairs M residual displacement vectors represented as matrices s

$$\mathbf{\Theta}_n = \begin{pmatrix} x_1 - x_{1_0} & y_1 - y_{1_0} \\ \vdots & \vdots \\ x_M - x_{M_0} & y_M - y_{M_0} \end{pmatrix} \tag{55}$$

referring to a set of M grid-like arranged control points can be obtained. The displacements are computed in analogy to (22). The mean residual deviation of a series is summed and normalized as

$$\epsilon = \frac{1}{(N-1)M} \sum_{n=1}^{N-1} \sqrt{\operatorname{trace}\left(\mathbf{\Theta}_n^{\top} \mathbf{\Theta}_n\right)}. \tag{56}$$

Although reflecting not only literal registration errors (of course, the goal is not to eliminate *any* differences of adjacent slices), in all of the 13 cases this error effectively can be further decreased by means of the second and third registration step. Note the numbers put in parentheses in the third "mean residual deviation" column of Table I: these were the mean residual registration deviations if the polynomial nonlinear registration would

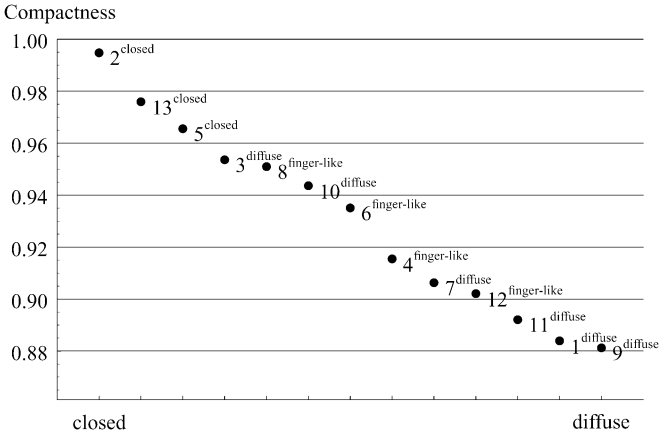

Fig. 17. The compactness values of the 3-D reconstructed specimen exhibit a rather homogeneous but not a three-tiered distribution as used for the verbal assessments (compare Fig. 2). Specimen 2 and 9 holds the most and least compactnesses, respectively. Dots are labeled with consecutive specimen numbers (see Table I). The terms next to the specimen numbers are from the pathologist's second assessment, while the abscissa has no other meaning than to qualitatively rank the compactness numbers.

be skipped evidencing how the processing chain benefits from this step.

The compactnesses for all specimen are rather equally distributed between 0.881 (diffuse invasion) and 0.995 (closed invasion, see, also Fig. 17). A corresponding linear regression with a verbal three-tiered 2-D based clinical routine assessment (cf. Table I) based on single slices out of the same specimen yielded a correlation coefficient of 0.73. One should note, however, that this is not a correlation with some hard reference, but illustrates that the new results are in a reasonable relation with the "traditional" ones, while being far superior concerning their degree of reliance. As the decisive benefit of the compactness-based quantification now these numbers can be used for clear more precise comparisons with other clinical parameters, as the expression of immunohistochemical markers or the survival period etc. To do the latter is still to early, while the first is ongoing work.

V. Discussion

Our method could successfully be applied. However, we want to emphasize why this processing chain is legitimate for the 3-D reconstruction process. In the following, we try to discuss aspects of known previous work in this or related fields.

Ourselin *et al.* [11] have introduced some single-step algorithm for the reference-free 3-D reconstruction of a rat's brain from serial sections, whereas we have set up a multistep processing scheme. Their implicit assumption is that after some rigid registration remaining distortions are not too important for the 3-D reconstruction, which is basically not considered acceptable for our work. However, applying some nonlinear registration on our data without assuring that throughout the slides the image correspondencies are accessible (irrespective the inherent differences between adjacent sections) would cause lots of severe problems. That is why an initial rigid registration step is considered essential, otherwise we would risk the failure of the following nonlinear steps. So we indeed have decided to keep the rigid step as simply as possible as well as slice-globally as possible. However, what was even more crucial is the magnitude at hand of the shifts/rotations to compensate, so the required block size would be quite large to sufficiently cover the appearing dislocations. In summary, these aspects have tipped the scales toward taking a nontiling approach for the rigid step. Ourselin *et al.*'s block-matching strategy applied for some basically more sophisticated rigid registration approach has some similarities to the image tiling setup for our second (polynomial) registration step. Besides the worthwile multiresolution implementation, they use a Manhattan distance based regression (L_1 norm) which has turned out to be more robust against (even some small portion of) outliers among the displacement vectors. The LS original (L_2 norm) in general is known to be decisively affected from outliers [48]. However, unlike LS, their regression requires numerical solution methods. Constrasting to Ourselin *et al.*'s work, outlier-induced problems have not been an issue in our work, neither we have got unwanted warpings with our setup (even with polynomials of fifth degree) nor we were in need to treat *all* distortions with the polynomial registration step.

Bardinet *et al.* [12] have reconstructed parts of the human brain (basal ganglia) using histological serial sections but could benefit from the existence of a reference incident light photographs data set which was taken just before sectioning. The registration algorithm is in principle that from [11] but applied as coregistration. As we would highly appreciate a reference data set for our work, we do not have, so we respect that the 3-D integrity of the results can be guaranteed. However, without some nonlinear registration step we have doubts that the result is satisfactory.

Basically, for our work we have had plans to provide us with some reference data just by taking incident light photographs from the cutting area immediatly before the respective microtome cut was obtained, as done by Schormann *et al.* [14]. However, this could not be applied for our data, since the general contrast was far too low to reasonably use them as reference pictures. In particular, looking on the unstained specimen one cannot reliably distinguish tumor from normal tissue. For example, the dark structures visible in Fig. 3 on the cutting area are not necessarily the tumor and have no correspondence which reliably can be found on the HE-stained sections. For the tumor-related reconstruction and analyses staining is essential, but it can only applied on the sliced tissue, not on the tissue block embedded in paraffin. Contrasting to the vast majority of papers reporting on histological serial section reconstructions we cannot exploit the availability of a more or less clearly visible structures (e.g., some organ outline), since on the microscope used for digitization we cannot capture the full slice ($\approx 4\ \mathrm{cm}^2$) but only some limited FOV of about 1 cm^2. Our images always cover some ROIs *amidst* the sections. Even if we would have covered (at least parts of) the organ outline, this would be a too weak reference for our data of interest which is the tumour invasion front. Schormann *et al.* [14] have treated the problem of 3-D reconstructing the human cortical brain from histological serial sections and could utilize both an incident light data set as well as a MRI 3-D data set (even though not coplanar to those of the other two). Moreover, they did scan the whole sections which

points to the important aspect that their work operates two orders of magnitude above our's, i.e., with voxels of about 1 mm extent—even though the microtome sectioning was done with 30 μm thickness. This and the Nissl staining has allowed them to register the incident light data with the slices. Instead, for our work it has turned out that in un-stained (in reference to HE) and unsectioned tissue no relevant tumor structures essential for use as reference are visible. What is common to our work is that the processing was done in steps doing first a affine registration (extended principal axis transform) and following some nonlinear elastic registration.

For Mega *et al.*'s paper [15] we have to state something very similar as for Schormann's. Besides utilizing a reference data set available (FDG-PET in this case), they also benefit from the incident light photographs taken before the physical sectioning, and again, they process full human brains with a spatial resolution in the order of 0.5 mm. What is especially interesting in this paper is that the 2-D-registrations (stained histological section onto the presectioning photo) were accomplished using pairs of correspondingly drawn contour sections along the brain outline which serve as registration anchors which are required from the elastic registration algorithm. It has to be assumed that this explicit focussing on the outline was done mainly due to contrast deficits within the tissue. As stated above, for our work we cannot exploit the specimen outline.

In [17], Ali and Cohen try to map 2-D histological sections onto an existing 3-D atlas of the rat's brain. The problem is treated as some outline based approach and utilizes geometric curve invariants (i.e., some inflection points) which are taken as kind of landmarks for the affine transform. Even if operating on a ≈ 20 μm scale this outline focussed approach is not at all appropriate for us. The outline is not included in our images, and the outline is an intuitive but weak anchor since it is frequently damaged from the microtome sectioning.

Last but not least, since additional lighting fluctuations are no matter here, since we can assure reproducible conditions on the microscope. The question is rather if it is maintainable to especially treat those staining fluctuation within our framework. Malandain and Bardinet [49] are addressing the related problem of intensity fluctuations along serial sections. Besides the central aspect of that paper, the smoothing of the discrete probability density function (PDF) obtained from the discrete histograms, it is crucial being capable to invert the respective error functions, which is no problem for the one-dimensional case. For three dimensions, however, this is no longer straightforward, as long as the PDF is not a (multivariate) Gaussian, so that the correction scheme proposed in [49] would be much more complicated. Having said that, to treat the three bands of RGB-images as independent scalar images to circumvent this would not be a good idea because this would ignore the vectorial character of the data.

Lehmann *et al.*'s work [16] is introducing the cepstrum technique into the Fourier-Mellin based rotation-, scaling-, and translation-invariant image descriptor, which among others is applied on histological images. It is closely related to the scheme we are applying for the rigid registration. Their main argument for doing this with the cepstrum technique is the robustness against uncorrelated noise and intensity distortions. The latter, however, is not a problem for our data. Moreover, even though the Fourier-Mellin technique as basically applied for our work too is capable to treat image scalings, there is no certain reason that the sections would be affected by forces requiring scaling to compensate them. All relevant image acquisition parameters including magnification were kept constant. Even if some slight shrinking or stretching of some sections would appear, this would be be treated as a special (isotropic) case of distortion later on and can be compensated by the nonlinear polynomial registration.

Fischer and Modersitzki [34] do present a very interesting work, a nonrigid image registration algorithm. This curvature-based nonlinear registration was adopted within this work for the third registration step. What is claimed is the needlessness of some rigid preregistration step as applied in various other approaches. As this might hold true for cases where the whole sections are visible, for our cases with even an initial FOV from within the sections this is not applicable. This means, in case of too much inexistent correspondencies, that algorithm will introduce unwanted warpings. That is why we have introduced some preregistrations. The reason why we did not just the rigid one but also the polynomial is that we wanted to act as careful as possible to avoid the loss of the 3-D integrity. However, what now seems to be worthwhile is to skip the polynomial registration in future, even though our results suggest to keep it, because we expect a further improved performance of the curvature registration if applied as multigrid scheme.

Compared to these sketched known related approaches, our conditions are probably more complicated, especially because of the absence of a reference data set. Another point is the use of a microscope for digitization which decisively restricts the FOV, but on the other hand is guaranteeing utmost reproducibility in lighting and optical accuracy at a "nominal" resolution of 3160 dpi (8.04 μm per pixel). A motorized table was unfortunately not available to us, however accurate stitching not necessarily would be trivial. Under the given conditions, we do not see alternatives as with the dedicated multistep scenario for tissue reconstruction aiming to preserve the structures of interest, i.e., the tumoral invasion fronts.

Form our point of view, our contribution might be considered as some preparation toward a virtual microscopy framework for histology and pathology. The upcoming purely digital microscopy technology sounds appealing for problems like our's. Products like MiraxScan by Zeiss or CoolScope by Nikon, to mention just two, are available meanwhile and can reach pixel extents down to 0.25 μm which corresponds to about 100 000 dpi. Those can operate at FOVs up to the full (!) glass slide at $1'' \times 3''$ using some built-in automatic image stitching. Resolution, however, is important but is not the only criterion. For example, for our 3-D reconstructions, we have been operating not far below the 2 GB RAM usage level. Even in future, irrespective of the most appropriate resolution which for our problem is about 3000 dpi, for this kind of problems one probably will operate in ROIs rather than within the whole respective FOV.

VI. Conclusion

With the above detailed scheme an objective quantification of the invasion of cervical tumors based on 3-D reconstructed

data could be achieved for the first time. To reach this main objective firstly we had to set up a dedicated image processing chain enabling us to provide a very detailed tissue reconstruction. The reason why transmitted light microscopy instead of flatbed scanning was used for this work is just to assure an excellent reproducible image quality at a required minimum resolution.

Our primary interest was not to extend a 2-D microscopic technique to 3-D, but to suffice a requirement of providing spatial resolutions of approx. 0.1 μm^{-1} using a well established modality which reliably can be utilized to segment the tumor. At present, even though desirable, due to computer memory limitations not even tumor stage T1b1 cervical carcinoma volumes can completely be reconstructed at this resolution. Self-evidently, the trade-off we found was just to select a typical region within the tumor invasion front which is considered to be representative for the whole respective tumor. Although we hardly can proof the latter—we rarely can accomplish a (tile-wise) reconstruction for a whole specimen—we consider that the obtained compactnesses are of particular interest for new detailed assessments of various prognostic factors of carcinoma of the uterine cervix.

The scheme we have introduced emphasizes 3-D, but requires a very extensive procedure. What will be subject of further investigations is the possible applicability of the discrete 2-D compactness referring to single sections as an alternative solution. Possibly, satisfactory conclusions from 2-D to 3-D compactness-based assessments can be made so that the expensive 3-D reconstruction can be circumvented for clinical routine.

ACKNOWLEDGMENT

The authors are indebted to R. Scherling who carefully accomplished all sectioning and staining essential for this work. They thank MICROM GmbH for kindly providing them with the electrically cooled object clamp "Cool-Cut" and the section transfer system "STS," both decisively facilitating and improving the sectioning of the large histological serial sections throughout this work. They would also like to thank T. Frohn for the digitizations. Finally, the authors would like to thank the referees for their careful and constructive suggestions.

REFERENCES

[1] L.-C. Horn, U. Fischer, and K. Bilek, "Morphologic factors associated with prognosis in surgically treated cervical cancer," *Zentralblatt für Gynäkologie*, vol. 123, pp. 266–274, May 2001.

[2] J. Baltzer, K. J. Lohe, W. Köpcke, and J. Zander, "Histological criteria for the prognosis in patients with operated squamous cell carcinoma of the cervix," *Gynecologic Oncol.*, vol. 13, pp. 184–194, Apr. 1982.

[3] V. Maaßen, R. Dieckhoff, J. Baltzer, and G. Kindermann, "Risk of hematogenous metastasis of cancer of the uterine cervix," *Zeitschrift für Geburtshilfe und Frauenheilkunde*, vol. 54, pp. 656–661, Dec. 1994.

[4] G. B. Kristensen, V. M. Abeler, B. Risberg, C. Trop, and M. Bryne, "Tumor size, depth of invasion, and grading of the invasive tumor front are the main prognostic factors in early squamous cell cervical carcinoma," *Gynecologic Oncol.*, vol. 74, pp. 245–251, Aug. 1999.

[5] P. J. Tadrous. (2002) Methods for Imaging the Structure and Function of Living Tissues and Cells. [Online]. Available: http://www.bialith.com/Teaching/PathologyPG/BAMScHCInV.PDF

[6] B. Luck, K. Carlson, T. Collier, and K.-B. Sung, "Confocal microscopy [detecting and diagnosing cancers]," *IEEE Potentials Mag*, vol. 23, no. 1, pp. 14–17, Feb. 2004.

[7] S. M. Boles, H. Hricak, and P. Rubin, "Carcinoma of the cervix and endometrium," in *Oncologic Imaging*, 2nd ed, B. G. Bragg, P. Rubin, and H. Hricak, Eds. Philadelphia, PA: Saunders, 2002, ch. 26, pp. 523–548.

[8] Y. Okamoto, Y. O. Tanaka, M. Nishida, H. Tsunoda, H. Yoshikawa, and Y. Itai, "MR imaging of the uterine cervix: Imaging-pathologic correlation," *Radiographics*, vol. 23, no. 2, pp. 425–445, Mar. 2003.

[9] C. Levinthal and R. Ware, "Three dimensional reconstruction from serial sections," *Nature*, vol. 236, pp. 207–210, Mar. 1972.

[10] S. J. Young, S. M. Royer, P. M. Groves, and J. C. Kinnamon, "Three-dimensional reconstruction from serial micrographs using the IBM PC," *J. Electron Microsc. Tech.*, vol. 6, pp. 207–217, 1987.

[11] S. Ourselin, A. Roche, G. Subsol, X. Pennec, and N. Ayache, "Reconstructing a 3-D structure from serial histological sections," *Image Vis. Comput.*, vol. 19, no. 1–2, pp. 25–31, Jan. 2001.

[12] É. Bardinet, S. Ourselin, G. Malandain, D. Tande, K. Parain, N. Ayache, and J. Yelnik, "Three dimensional functional cartography of the human basal ganglia by registration of optical and histological serial sections," in *Proc. IEEE Int. Symp. Biomedical Imaging (ISBI'02)*, Washington, DC, Jul. 2002, pp. 329–332.

[13] T. Schormann and K. Zilles, "Limitations of the principal-axes theory," *IEEE Trans. Med. Imag.*, vol. 16, no. 6, pp. 942–947, Dec. 1997.

[14] ——, "Three-dimensional linear and nonlinear transformations: An integration of light microscopical and MRI data," *Hum. Brain Mapp.*, vol. 6, no. 5–6, pp. 339–347, 1998.

[15] M. S. Mega, S. S. Chen, P. M. Thompson, R. P. Woods, T. J. Karaca, A. Tiwari, H. V. Vinters, G. W. Small, and A. W. Toga, "Mapping histology to metabolism: Coregistration of stained whole-brain sections to premortem PET in Alzheimer's disease," *Neuroimage*, vol. 5, no. 2, pp. 147–153, Feb. 1997.

[16] T. M. Lehmann, C. Goerke, A. Kaupp, W. Schmitt, and R. Repges, "A rotation-extended cepstrum technique and its application to medical images," *Pattern Recognit. Image Anal.*, vol. 6, no. 3, pp. 592–604, 1996.

[17] W. S. I. Ali and F. S. Cohen, "Registering coronal histological 2-D sections of a rat brain with coronal sections of a 3-D brain atlas using geometric curve invariants and B-spline representation," *IEEE Trans. Med. Imag.*, vol. 17, no. 6, pp. 957–966, Dec. 1998.

[18] J. B. A. Maintz and M. A. Viergever, "A survey of medical image registration," *Med. Image Anal.*, vol. 2, pp. 1–37, Mar. 1998.

[19] F. Maes, D. Vandermeulen, and P. Suetens, "Medical image registration using mutual information," *Proc. IEEE*, vol. 91, pp. 1699–1722, Oct. 2003.

[20] J. Modersitzki, *Numerical Methods for Image Registration*. New York: Oxford Univ. Press, 2004.

[21] L. H. Sobin and C. Wittekind, Eds., *TNM Classification of Malignant Tumours*, 6th ed. New York: Wiley, 2002.

[22] M. Höckel, L.-C. Horn, B. Hentschel, S. Höckel, and G. Naumann, "Total mesometrial resection: High resolution nerve-sparing radical hysterectomy based on developmentally defined surgical anatomy," *Int. J. Gynecological Cancer*, vol. 13, pp. 791–803, Nov. 2003.

[23] D. Casasent and D. Psaltis, "Position, rotation and scale-invariant optical correlation," *Appl. Opt.*, vol. 15, pp. 1795–1799, Jul. 1976.

[24] J. L. Horner and P. D. Gianino, "Phase-only matched filtering," *Appl. Opt.*, vol. 23, pp. 812–816, Mar. 1984.

[25] Q.-S. Chen, M. Defrise, and F. Deconinck, "Symmetric phase-only matched filtering of Fourier-Mellin transforms for image registration and recognition," *IEEE Trans. Pattern Anal. Machine Intell.*, vol. 16, no. 12, pp. 1156–1168, Dec. 1994.

[26] B. S. Reddy and B. N. Chatterji, "An FFT-based technique for translation, rotation, and scale-invariant image registration," *IEEE Trans. Image Processing*, vol. 5, no. 8, pp. 1266–1271, Aug. 1996.

[27] R. C. Gonzales and R. E. Woods, *Digital Image Processing*. Reading, MA: Addison Wesley, 1992.

[28] M. McGuire. (1998) An Image Registration Technique for Recovering Rotation, Scale and Translation Parameters. [Online]. Available: http://www.cs.brown.edu/people/morgan

[29] B. Cabral and L. C. Leedom, "Imaging vector fields using line integral convolution," in *Proc. SIGGRAPH '93)*, vol. 27, 1993, pp. 263–272.

[30] D. Stalling, "Fast texture-based algorithms for vector field visualization," Ph.D. thesis, Fachbereich Mathematik und Informatik der Freien Universität Berlin, Berlin, Germany, 1998.

[31] E. L. Hall, *Computer Image Processing and Recognition*. New York: Academic, 1979, ch. 4.3.1.

[32] L. G. Brown, "A survey of image registration techniques," *ACM Computing Surveys*, vol. 24, no. 4, pp. 325–376, Dec. 1992.
[33] Y. Amit, "A nonlinear variational problem for image matching," *SIAM J. Scientific Computing*, vol. 15, no. 1, pp. 207–224, Jan. 1994.
[34] B. Fischer and J. Modersitzki, "Curvature based image registration," *J. Math. Imag. Vis.*, vol. 18, pp. 81–85, Jan. 2003.
[35] M. Abramowitz and I. A. Stegun, *Pocketbook of Mathematical Functions*. Frankfurt, Germany: Verlag Harri Deutsch, 1984.
[36] P. Cachier and N. Ayache, "Regularization in Image Non-Rigid Registration: I. Trade-Off Between Smoothness and Intensity Similarity," The French National Institute for Research in Computer Science and Control (INRIA Sophia Antipolis), Res. Rep. 4188, 2001.
[37] ——, "Regularization Methods in Non-Rigid Registration: II. Isotropic Energies, Filters and Splines," The French National Institute for Research in Computer Science and Control (INRIA Sophia Antipolis), Res. Rep. 4243, 2001.
[38] P. Perona and J. Malik, "Scale-space and edge detection using anisotropic diffusion," *IEEE Trans. Pattern Anal. Machine Intell.*, vol. 12, no. 7, pp. 629–639, Jul. 1990.
[39] J. Weickert, *Anisotropic Diffusion in Image Processing*. Stuttgart, Germany: Teubner-Verlag, 1998.
[40] T. F. Chan, S. Osher, and J. Shen, "The digital TV filter and nonlinear denoising," *IEEE Trans. Image Processing*, vol. 10, no. 2, pp. 231–241, Feb. 2001.
[41] W. E. Lorensen and H. E. Cline, "Marching cubes: A high resolution 3-D surface construction algorithm," *Comput. Graphics*, vol. 21, no. 4, pp. 163–169, 1987.
[42] D. Moore and J. Warren, "Mesh Displacement: An Improved Contouring Method for Trivariate Data," Rice Univ., Houston, TX, Tech. Rep. TR91-166, 1991.
[43] ——, "Compact isocontours from sampled data," in *Graphics Gems III*, D. Kirk, Ed. Boston, MA: AP Professional, 1992, pp. 23–28.
[44] J.-P. Kuska, "Volume rendering with MathGL3d," in *Challenging the Boundaries of Symbolic Computation, Proc. 5th Mathematica Symp.*, P. Mitic, P. Ramsden, and J. Carne, Eds., 2003, pp. 341–348.
[45] ——, (1997–2005) MathGL3d—Interactive OpenGL viewer for Mathematica. [Online]. Available: http://phong.informatik.uni-leipzig.de/~kuska/mathgl3dv3/
[46] N. Singh and S. Arif, "Histopathologic parameters of prognosis in cervical cancer—A review," *Int. J. Gynecological Cancer*, vol. 14, no. 5, pp. 741–750, Sep. 2004.
[47] E. Bribiesca, "A measure of compactness for 3-D shapes," *Comput. Math. Applicat.*, vol. 40, pp. 1275–1284, Nov./Dec. 2000.
[48] P. J. Rousseeuw and A. M. Leroy, *Robust Regression and Outlier Detection*. New York: Wiley, 1987, ch. 5.4, pp. 208–214.
[49] G. Malandain and É. Bardinet, "Intensity compensation within series of images," in *Lecture Notes in Computer Science*. Berlin, Germany: Springer-Verlag, Nov. 2003, vol. 2879, Proc. Medical Image Computing and Computer-Assisted Intervention (MICCAI2003), pp. 41–49.